European Journal of Medicinal Chemistry 320 (2026) 119306

Contents lists available at ScienceDirect

European Journal of Medicinal Chemistry

journal homepage: www.elsevier.com/locate/ejmech

Research paper

A combination of MD-derived pharmacophores and structure-based strategy identifies dual allosteric inhibitors of NS2B-NS3 proteases in Zika and West Nile viruses

Antonio Lupia [a,1], Salvatore Nieddu [b,1], Laura Demuru [a], Erica Sanna [a], Alessia Onali [a], Roberta Emmolo [b], Paolo Malune [b], Simona Distinto [a,*], Giulia Atzeni [a], Annalaura Paulis [b], Rita Meleddu [a], Filippo Cottiglia [c], Francesca Esposito [b], Angela Corona [b], Sharon D. Bryant [d], Elias Maccioni [a], Enzo Tramontano [b,**]

[a] Department of Life and Environmental Sciences, Drug Sciences Section, Laboratories of Synthesis and CADD, University of Cagliari, A Building, University Campus, S.P. 8, Monserrato, CA, 09042, Italy
[b] Department of Life and Environmental Sciences, Biomedical Section, Laboratories of Molecular Virology, University of Cagliari, E Building, University Campus, S.P. 8, Monserrato, CA, 09042, Italy
[c] Department of Life and Environmental Sciences, Drug Sciences Section, Laboratory for the Extraction of Bioactive Compounds, University of Cagliari, A Building, University Campus, S.P. 8, Monserrato, CA, 09042, Italy
[d] Inte:Ligand GmbH, Mariahilfer Straße 74B/11, Vienna, 1070, Austria

ARTICLE INFO

Keywords:
Flavivirus
NS3
MD pharmacophores
Allosteric inhibition
Drug repositioning

ABSTRACT

Starting from the crystal structure of a Zika virus (ZIKV) NS2B-NS3 protease with bound allosteric inhibitor, we generated dynamic pharmacophore models derived from representative molecular dynamics (MD) conformations to capture key interaction patterns. These models guided a pharmacophore-based virtual screening of commercial libraries, including commercial compounds and approved drugs, enabling the rapid selection of virtual hit compounds. Biochemical evaluation identified several inhibitors, with the antiretroviral drug Nelfinavir emerging as the most promising compound. Nelfinavir displayed the strongest inhibition of ZIKV and West Nile virus (WNV) proteases and showed antiviral activity in cell-based assays, with EC_{50} values of 1.79 ± 0.01 μM on ZIKV and 3.01 ± 1.25 μM in WNV, supporting its relevance as a repositionable scaffold for modulation of ZIKV and WNV infections. The activity observed across flavivirus proteases highlights the value of targeting conserved allosteric regions. Overall, this integrated computer-aided drug design (CADD) strategy demonstrates the power of dynamic, structure-based pharmacophores to uncover novel allosteric inhibitors and accelerate antiviral drug repurposing.

1. Introduction

Zika virus (ZIKV) and West Nile virus (WNV) are mosquito-borne Flaviviruses from the Flaviviridae family, Flavivirus genus, which also includes Dengue virus (DENV), Yellow Fever virus (YFV), and Japanese encephalitis virus (JEV). ZIKV is primarily transmitted by Aedes species mosquitoes, including *Aedes aegypti* and *Aedes albopictus*, while WNV is spread by Culex species [1,2]. WNV and ZIKV have emerged as significant human pathogens. Particularly, ZIKV led to significant outbreaks in the Pacific and the Americas, prompting the WHO in 2016 to declare a Public Health Emergency of International Concern due to the rise in congenital and neurological issues [3]. Most cases are asymptomatic or mild, with symptoms like rash, fever, conjunctivitis, joint pain, and muscle aches appearing 3-4 days after infection and lasting up to a week. In pregnant women, infection can result in microcephaly and other congenital defects, while in adults, it has been linked to Guillain-Barré syndrome (GBS) and various neurological disorders [4–9]. WNV is now endemic in the Mediterranean basin and in the Americas, with a growing

* Corresponding author.
** Corresponding author.
E-mail addresses: s.distinto@unica.it (S. Distinto), tramon@unica.it (E. Tramontano).
[1] These authors contributed equally to this work.

https://doi.org/10.1016/j.ejmech.2026.119306
Received 21 April 2026; Received in revised form 27 June 2026; Accepted 2 September 2026
Available online 5 September 2026

number of cases [10,11]. While 80% of the cases are asymptomatic and most of the others show mild symptoms, < 1% develop a neuroinvasive disease leading to meningitis, encephalitis, or poliomyelitis [11]. Hence, both ZIKV and WNV are re-emerging global threats.

Both viruses have a positive-sense, single-stranded RNA genome of about 11 kilobases containing an open reading frame that is translated into a single polyprotein precursor. In the host endoplasmic reticulum (ER), the polyprotein is cleaved both co-translationally and post-translationally by the viral protease in the cytoplasm and by host proteases in the ER lumen. This process produces three structural proteins (capsid, pre-membrane, and envelope) and seven non-structural proteins. Among them, NS3 possesses protease activity in its N-terminal domain and helicase and NTPase activities in its C-terminal region [12]. The NS3 protease (NS3pro), in a complex with cofactor NS2B that contains essential transmembrane segments, is responsible for the cytoplasmic cleavages at the NS2A-NS2B, NS2B-NS3, NS3-NS4A, and NS4B-NS5 junctions [13]. The cleavage is regulated by a catalytic triad, involving histidine (H51), aspartic acid (D75), and serine (S135) at the NS2B-NS3 protease active site (Fig. 1).

The NS2B-NS3 protease recognizes di-basic cleavage sites in the viral polyprotein and exists in two conformations: an 'open' form, which is inactive, and a 'closed' form, where the C-terminal region of NS2B forms a β-hairpin that stabilizes the S2 and S3 pockets, thereby activating the enzyme [14–16]. Of note, the enzyme is crucial not only for processing the viral polyprotein but also for cleaving host substrates, such as STING and JAK, to suppress innate immunity [17]. Overall, its essential role in the viral life cycle makes NS2B-NS3 a key target for antiviral drug development.

Despite extensive global efforts, there are no vaccines or approved antiviral treatments for ZIKV and WNV infections [18–20]. Focusing on NS2B-NS3, several major obstacles have impeded the development of effective inhibitors. First, i) the shallow, flat, charged, and solvent-exposed nature of the catalytic site (Fig. 1, panel a) makes it especially difficult for small molecules to bind, potentially requiring unconventional scaffolds, peptidomimetics, macrocyclic compounds, or covalent inhibitors [21]; ii) the dynamic behavior of NS2B-NS3 protease, specifically its open and closed conformational states, and the flexibility of the linker region connecting NS3pro to NS3hel must be taken into consideration [22], and iii) the protease structure contains many charged residues (Fig. 1, panel b), particularly near the active site, resulting in very low target druggability [18–20]. Considering these limitations, targeting the NS2B-NS3 protease allosteric cavity instead of the active site may be a more effective approach for rational drug design [21]. This allosteric pocket is more hydrophobic and less flat and charged than the solvent-exposed catalytic site, which increases the chances of forming well-defined buried regions. Additionally, conformational changes could reveal or create transiently buried subpockets, thereby offering a more favorable environment for ligand binding.

In this study, we applied a rational CADD strategy combining conventional molecular dynamics (cMD) simulations with the generation of

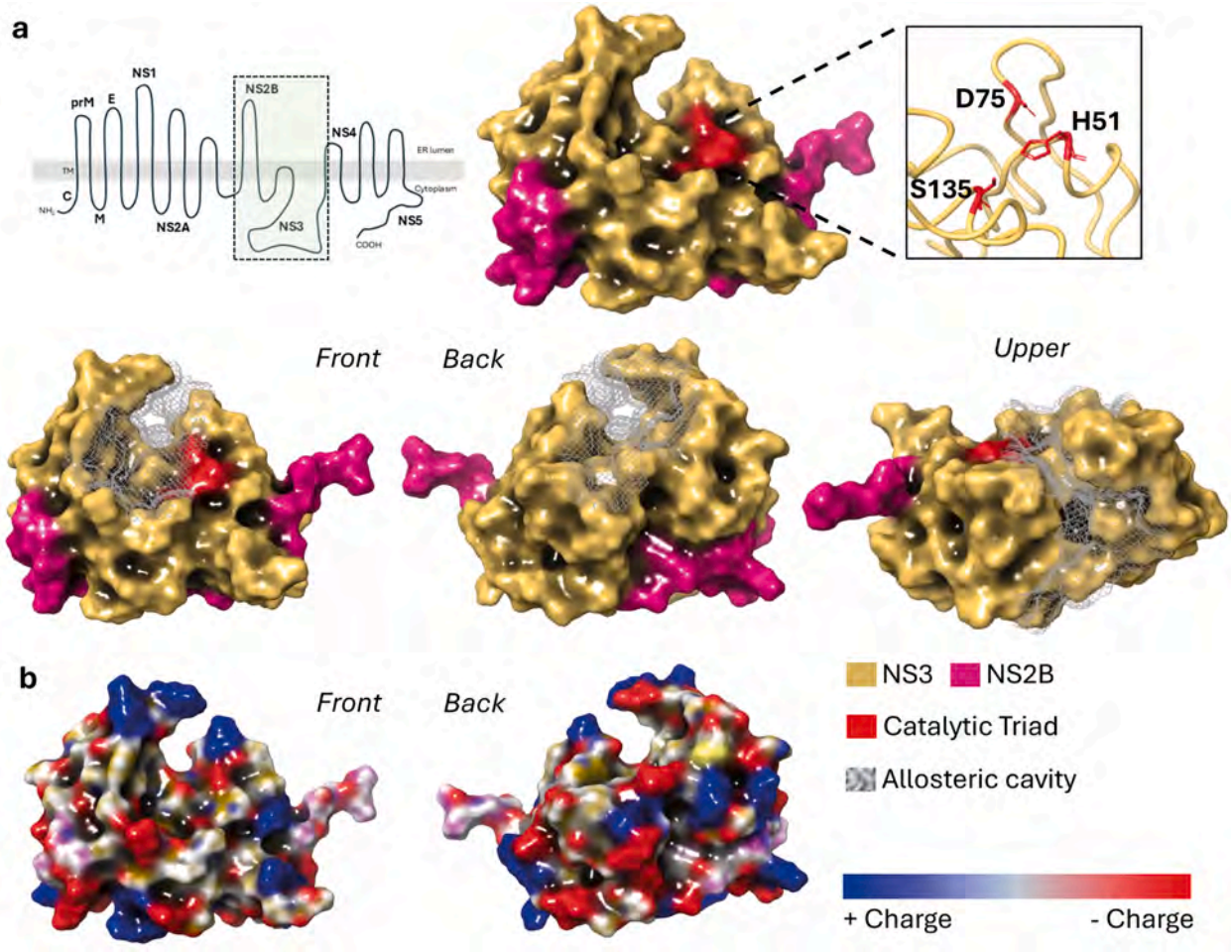

Fig. 1. Overview of NS2B-NS3 protease. a) Plot of the flaviviral NS2B-NS3 protease (ZIKV structure shown) polyprotein across the ER, with a detailed surface view of the NS2B-NS3 protease, highlighting the catalytic triad and the mapped allosteric cavity (grey mesh) from different angles. b) The protease surface area, with many positive and negative charged regions, is colored in red and blue, respectively. The images were created using Maestro GUI and X-ray resolved model (PDB ID: 7M1V).

Representative Pharmacophore Models (RPMs) derived from cMD. Using different libraries, including SPECS and FDA-approved drugs (totaling 201.839 compounds), we performed a Pharmacophore-Based Virtual Screening (PBVS) campaign against NS2B-NS3 protease. Sixteen promising hits were then tested for their ability to inhibit the enzymatic activity of ZIKV and WNV NS2B-NS3 protease in vitro. The most promising compounds **3**, **4**, **7**, and **16** were further investigated for their capacity to block the viral replication in a cell-based assay, with the FDA-approved drug Nelfinavir emerging as a potent inhibitor of ZIKV and WNV replication.

These results demonstrate the potential of targeting non-canonical, dynamically accessible regions of the protease and supporting drug repurposing as a promising approach to developing antiviral treatments against flaviviruses.

2. Results and discussion

2.1. Computational studies

After a thorough review of bibliographic and structural databases, no experimentally resolved NS2B-NS3 protease structures from WNV with allosteric inhibitors in the Protein Data Bank (PDB) were found. Most WNV NS2B-NS3 structures in these databases are either complexed with peptides or active-site inhibitors (such as PDB IDs: 2IJO [23] and 5IDK [24]) or ligand-free crystal structures. Therefore, our initial computational study focused on the ZIKV protease, for which instead, a complex structure is available. Importantly, analyses of structural and sequence conservation showed that NS3pro ZIKV and WNV proteases share 67% sequence identity and 80% similarity, supporting the relevance of ZIKV also as a structural surrogate for WNV in early-stage computational studies (see Supplementary Data (SD): Fig.s S1-S2 and Table S1).

2.1.1. Parsing ZIKV NS2B-NS3 protease models and target optimization

A customizable Konstanz Information Miner (KNIME) workflow, based on a previously released one on the KNIME Hub (hub.knime.com/s/x-AgotAUri5-inAe), was created to collect, analyze, and process data related to ZIKV NS2B-NS3 protease models (Fig. 2, panel a). This workflow enabled automated retrieval, annotation, and preprocessing of protease models for subsequent computational analyses.

The KNIME Analytics Platform is an open-source, user-friendly platform widely used across various research fields, where algorithms for processing data are wrapped in KNIME extensions provided by KNIME or other academic and/or commercial providers, enabling data management, visual assembly, and interactive execution of workflows in a plug-and-play fashion [25]. It also enables the creation of custom nodes and the integration of scripts written in various programming languages for statistical analysis, visualization, and the investigation of biological data. In medicinal chemistry, KNIME provides extensions and workflows to simplify the efficient and systematic retrieval of target protein and ligand data from multiple publicly accessible databases, including the PDB, PubChem, and ChEMBL. This feature enables the quick compilation of comprehensive datasets that combine structural, biochemical, and pharmacological information, which is essential for structure-based drug discovery. Notably, its modular node architecture enables automated querying, filtering, and data extraction using user-defined keywords and parameters, ensuring high reproducibility and reducing manual effort. Specifically, using the keywords "ZIKA virus", "Protease", and "NS2B-NS3", we retrieved 86 three-dimensional complexes (see SD: List-PDBs_ZIKV.csv). All structures were aligned on the protein backbone and visually inspected, with particular focus on the NS2B-NS3 protease allosteric pocket. Importantly, among all the retrieved PDB entries, most of the structures featured ligands bound within the catalytic site. Conversely, we specifically chose the model with accession code 7M1V [26] (Fig. 2, panel b), as it is the only available crystallographic structure of the ZIKV NS2B-NS3 protease in

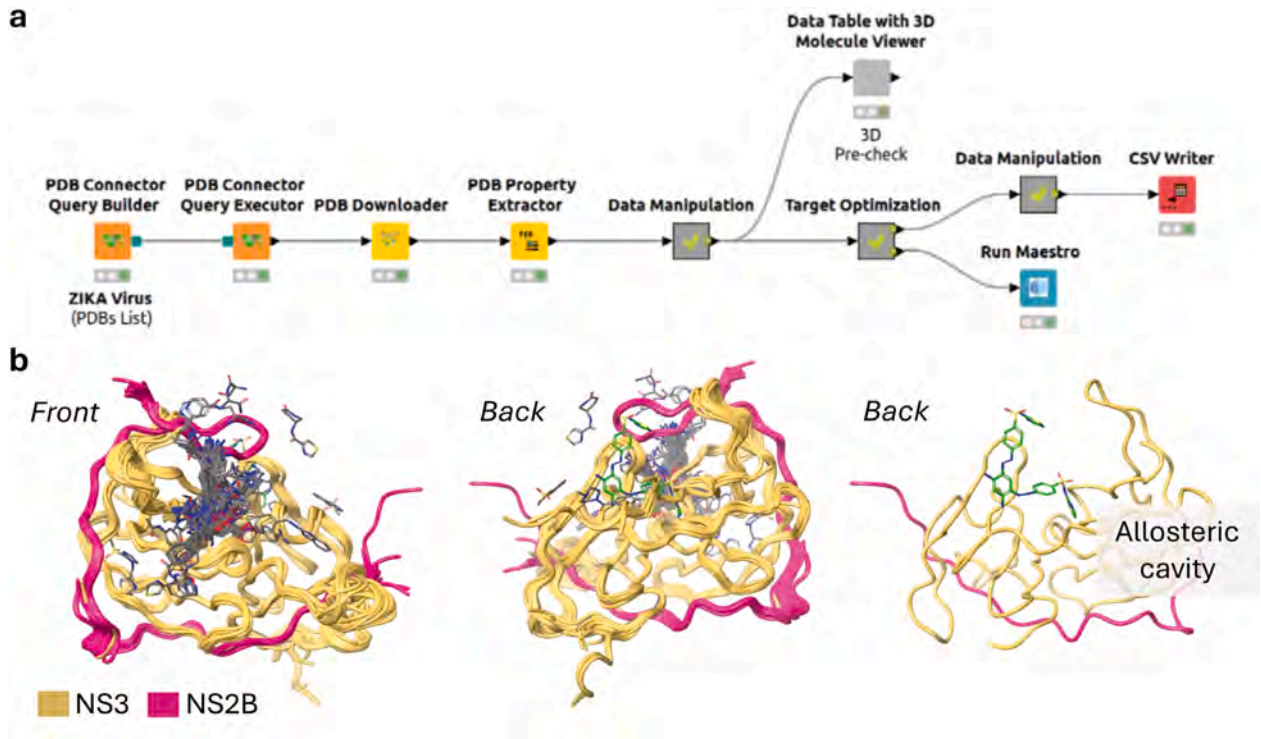

Fig. 2. a) A schematic KNIME workflow illustrating the process of querying, downloading, and processing ZIKV NS2B-NS3 protease structures from the PDB for target optimization and molecular modeling. The pipeline includes data extraction, manipulation, 3D molecular visualization, and preparation for docking simulations using Maestro software. b) Structural representations of the ZIKV NS2B-NS3 protease before and after data processing workflow. The yellow tube highlights the NS3 protease domain, while the magenta ribbon indicates the NS2B cofactor. Ligands are shown as stick models within both catalytic (in grey) and allosteric (in green) pockets, demonstrating their spatial arrangement and solvent exposure. Hydrogens are not displayed.

complex with a ligand in the allosteric site (at the beginning of the study). This structure is co-crystallized with the non-peptidic inhibitor NSC86314, which shows potent, low-micromolar activity against ZIKV NS2B-NS3 protease ($IC_{50} = 1.12 \pm 0.11$ μM), WNV, and DENV2 [13,27].

2.1.2. Assessment of NSC86314-ZIKV NS2B-NS3 protease complex stability and representative pharmacophore models (RPMs) generation

To execute an advanced virtual screening (VS) strategy, we used LigandScout 4.5 Expert to derive representative 3D-pharmacophores from all-atom classical molecular dynamics (MD) simulations of ZIKV NS2B-NS3 protease in complex with the inhibitor NSC86314. Initially, to gather insights into conformational changes and key molecular interactions in the NSC86314-ZIKV NS2B-NS3 complex, two independent MD simulations (1 μs each) were conducted in aqueous solution. Results indicated excellent protein stability (*P*-RMSD), with average backbone deviations of 1.70 Å and 1.37 Å for Run1 and Run2, respectively (Fig. 3). Meanwhile, a significant conformational rearrangement in the ligand (*L*-RMSD) was observed, as compared to the initial crystallographic pose. Therefore, MD trajectories were clustered to identify the most representative structure (cluster c0). In RMSD calculations, the atoms included were the protein backbone (*P*) and the heavy atoms of the ligand (*L*). Despite the observed ligand flexibility, the examination of the four aligned clusters (alignment scores: P-c0, Run1 vs P-c0, Run2 = 2.89 Å; L-c0, Run1 vs L-c0, Run2 = 5.76 Å) indicates that NSC86314 consistently maintained the same orientation within the allosteric cavity (Fig. S3), underscoring the robustness of the interaction pattern.

At this stage, the LigandScout 4.5 Extensions for KNIME were used to create a workflow to generate, analyze, and extrapolate the Representative Pharmacophore Models (RPMs) from each MD trajectory (Fig. 4, panel a). However, it is worth noting that the flexibility of the ligand during MD introduces heterogeneity in RPMs. Specifically: a) the ligand was co-crystallized in an allosteric site that is quite exposed to the solvent; b) it exhibited flexibility due to rotatable bonds in its structure. Therefore, the advantage of using RPMs is that they can identify more 3D-pharmacophoric interaction patterns in the allosteric site by considering conformational changes, thereby potentially increasing the success rate of hit discovery during the VS step, which is possibly limited by the static (X-ray derived) SB-pharmacophore model alone. In addition, it can highlight the common chemical features associated with specific amino acid binding partners based on their percentage of occurrence (%App) (Fig. 4, panels b-c). The analysis of the extrapolated RPMs from the NSC86314-ZIKV NS2B-NS3 protease complex revealed dominant hydrophobic (H) contribution involving residues, such as, W69, L76, W83, L85, I123, L149, and V155, as well as several hydrogen bond donors (HBDs) features, including D86, I147, and N152. Notably, the aromatic feature of the static pharmacophore (derived from the minimized X-ray resolved structure) was absent in both RPMs. Exclusion volume spheres (XVOLs) were added automatically by LigandScout to structure-based pharmacophores and were considered in all the 3D-pharmacophore hypotheses.

Next, an *in silico* validation of the prioritized structure-based pharmacophore models was carried out by downloading from ChEMBL [28,29] a dataset of ligands tested at NS3 (Target ID: 4523954) and virtually screening the dataset with the models. Compounds with reported IC_{50} values were divided into active and inactive groups and considered into LigandScout virtual screening libraries in order to be screened with the models. The screening results were used to generate the Receiver Operating Characteristic (ROC) curves, which visually shows sensitivity (true positives rate, TPR) as a function of the false-positive rate (false positives, FPR) (1 − specificity) (Table S2). Essentially, if the area under the curve (AUC) approaches one, it indicates that the pharmacophore

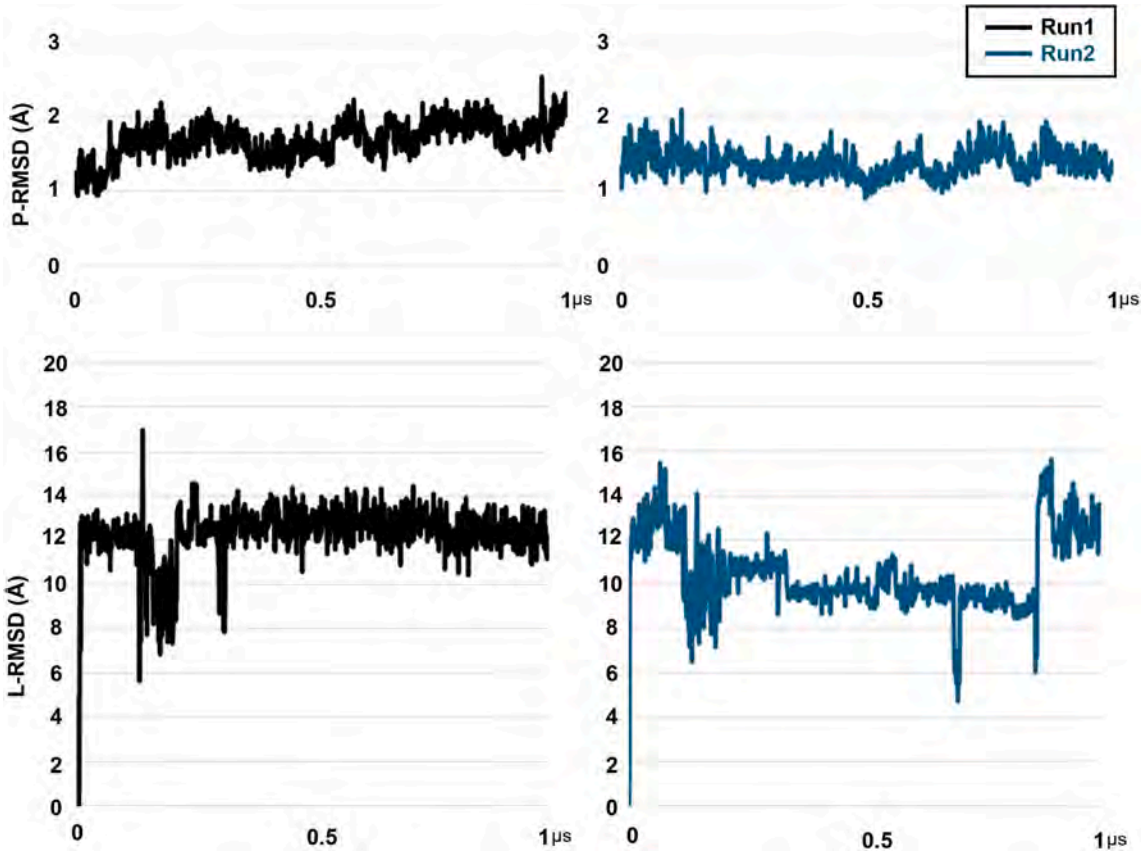

Fig. 3. All-atom protein (*P*-) and ligand (*L*-) RMSD plots of the NSC86314-ZIKV NS2B-NS3 protease complex derived from two independent molecular dynamics (MD) runs.

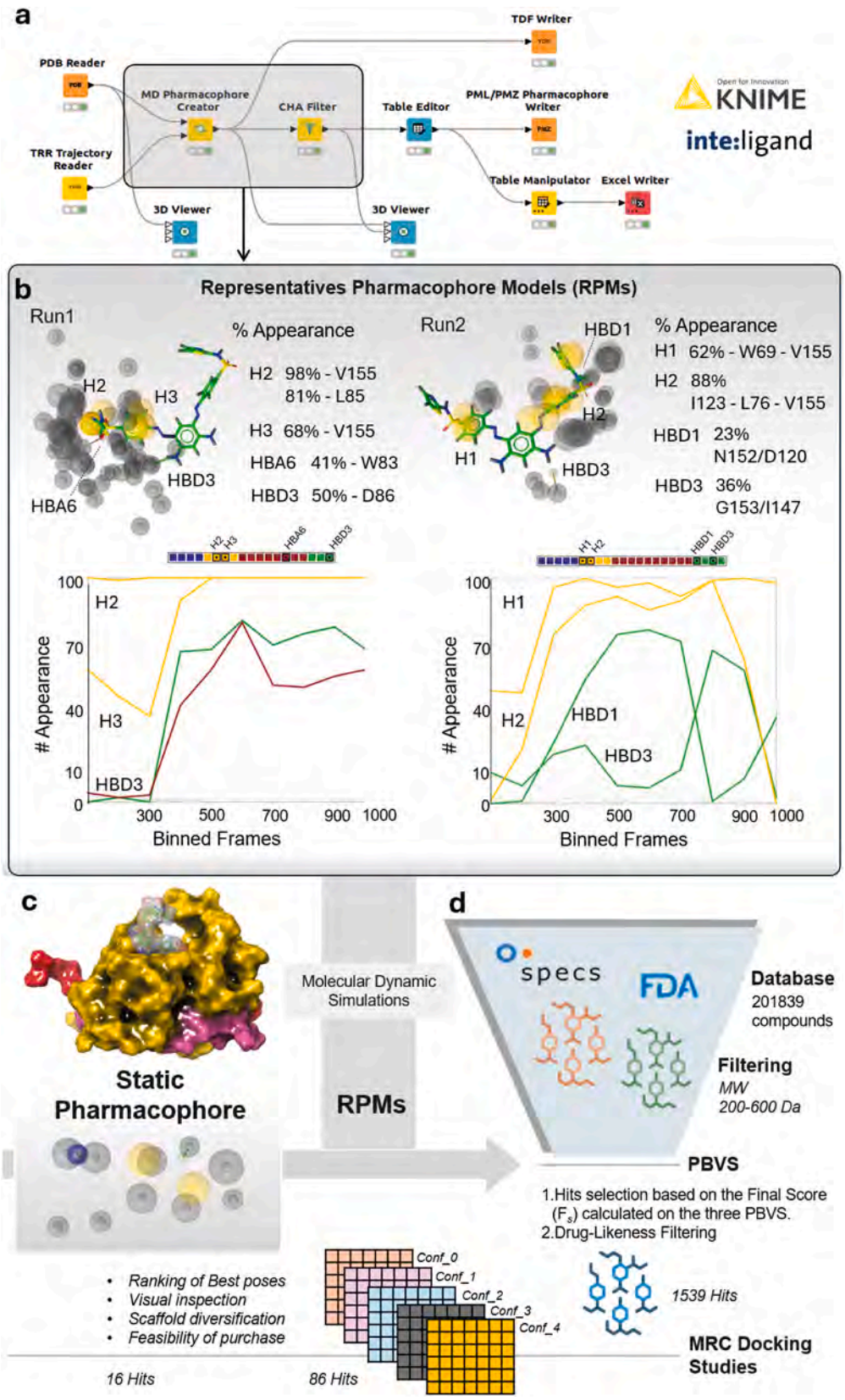

Fig. 4. Schematic overview of the *in silico* pipeline. a) KNIME workflow using LigandScout Extensions for KNIME; b) RPMs and feature frequency appearance plots, showing the Representative Pharmacophore Models and interaction patterns are represented as percentage of time that an observed chemical feature was associated with the same binding partner with the most involved residues highlighted. H, HBD, and HBA refer to the hydrophobic, hydrogen-bond donor, and hydrogen-bond acceptor pharmacophore features, respectively. c) The Static pharmacophore extracted from the minimized complex (PDB ID: 7M1V). d) Schematic diagram of the filtering step, PBVS, and MRC docking approach. The total number of hits for each stage is shown.

model reliably distinguishes active compounds from inactive ones. Results from the validation of the static-hypo pharmacophore model showed a smooth, progressive enrichment, it reliably separates actives from inactive compounds throughout the ranked list, with the AUC increasing from 0.70, 0.81, and 0.88 at the 1%, 5%, and 10% thresholds, respectively, and an overall AUC100% of 0.61. The sensitivity index was estimated at 66%, with more than half of the active compounds successfully identified. The RPM1-hypo-model yielded AUC values of 0.94, 0.77, and 0.57 at 1%, 5%, and 10% thresholds, respectively. It displayed a strong early enrichment profile, indicating that the model selected a high number of actives at the very top of its ranked output. However, the AUC declined progressively to 0.57 at 10%. Despite a lower overall AUC100% of 0.47, the sensitivity index was estimated at 52%, with over half of the active compounds detected. This profile is characteristic of a model with high specificity but limited coverage. Finally, the RPM2-hypo-model demonstrated the strongest overall validation profile among the three models, with AUC values of 0.99, 0.81, and 0.80 at the 1%, 5%, and 10% thresholds, respectively, resulting in an overall AUC100% of 0.65 and a sensitivity index of 60%. Hence, it achieved near-perfect early enrichment while maintaining consistently high discriminatory power as the ranked list was extended. Unlike models that recover actives rapidly but lose performance in later fractions, RPM2-hypo sustained a robust AUC across all thresholds. Given the high early enrichment results of the three models and the combination with subsequent docking experiments, the prioritized 3D pharmacophore models were used in the VS and served as queries for PBVS against a commercial library, SPECS, and FDA-approved drugs, totaling 201,839 compounds (Fig. 4, panel d).

2.1.3. Pharmacophore-based virtual screening (PBVS) campaigns and hits selection based on Multiple Receptor Conformation (MRC) docking studies

Virtual hits from the pharmacophore-based screening were scored and ranked by pharmacophore fit scores. To further support the selection of hits for experimental assays, we integrated complementary approaches, such as pharmacophore scoring and molecular docking, in a consensus scoring approach, which has been widely adopted to improve hit identification and reduce false positives [30]. Several studies have shown that combined screening strategies, applied either in parallel or sequentially, outperform individual methods by leveraging their complementary strengths and enhancing enrichment of active compounds [31–34]. Hence, to prioritize candidates for biological evaluation, the following criteria were used: a) compounds identified through the PBVS process were assigned values in terms of a Final Score (Fs) equal to 1 (best), 0.8 (average), and 0.6 (poor), depending on whether they appeared in all three PBVS rounds, two, or only one, respectively (SI:02-PBVS-MCR_data). As a result, a library of 1539 compounds was assembled, including 33 FDA and 1506 SPECS molecules; b) the selected candidates were screened via molecular docking onto the allosteric site of ZIKV NS2B-NS3 protease complex, using different receptor conformations, a process known as the Multiple Receptor Conformation (MRC) docking approach [35,36]; c) for the final selection, compounds with an average energy profile below −5.5 kcal/mol were considered, along with other parameters such as drug-like properties, chemical scaffold diversity, and, most importantly, the commercial availability and ease of procurement process of the compounds. Out of 86 candidates, 6 FDA and 10 SPECS hits were selected for purchase and biological testing (Fig. 5).

Chemically, the six selected FDA-approved drugs are characterized by a quinoline-based core in Cabozantinib (**1**), an imidazole containing biphenyl tetrazole scaffold shared by Losartan (**2**), and Olmesartan (**5**), a hydroxyethylamine-based peptidomimetic framework in Nelfinavir (**3**), a 2-phenylaminopyrimidine scaffold in Nilotinib (**4**), and a benzylaminoacetamide-based benzilamine scaffold in Safinamide (**6**). The ten compounds retrieved from the SPECS commercial database display a wide range of heterocyclic and aromatic scaffolds. Compound **7** (AH-487/13431101) features a 3a,4,5,9b-tetrahydro-3H-cyclopenta [c]quinoline core, while compounds **8** (AK-968/15610123) and **9** (AN-212/13751224) are furan and fluorenyl derivatives, with the latter functionalized with a hydroxyl group at the C9 position. Compound **10** (AN-465/41988204) contains a diphenylmethylamine scaffold, whereas compound **11** (AO-022/43452798) is characterized by a triazolophthalazine core. Additional structural variation is offered by compound **12** (AO-022/43453921), which exhibits a furo[3,2-g]chromene-7-one framework, and compound **13** (AO-080/42576167), which features a 1,2,4-triazole ring. Compound **14** (AP-906/41648836) presents a fused quinoline-pyrimidine heterocycle with two dione functionalities that confer structural rigidity. Furthermore, compound **15** (AR-434/42807203) displays a tricyclic heteroaromatic system, where a pyridine ring is fused with thiophene and pyrimidine moieties, and includes a carbonyl group at the 4-position. Finally, compound **16** (AS-871/43348421) contains a 1,3-thiazole ring as its structural motif.

2.2. Biological studies

2.2.1. Evaluation of compounds on ZIKV and WNV NS2B-NS3 enzyme activities

The sixteen identified compounds (Fig. 5) were tested for their ability to inhibit both ZIKV and WNV NS2B-NS3 enzymatic proteases activity using a fluorescent proteinase activity assay (Table 1, Fig. S4–S5) with Aprotinin and Temoporfin as validated positive controls [27,37]. Results showed that compounds **3**, **7**, and **16** inhibited the ZIKV NS2B-NS3 protease activity with IC_{50} values below 30 μM, whereas compound **4** retained inhibitory activity only at higher concentrations. Notably, the FDA-approved compound **3** (Nelfinavir) exhibited the most potent inhibitory effect against the ZIKV NS2B-NS3 protease, with an IC50 value of 13.5 μM. Of note, compound **3** (Nelfinavir) emerged as the most potent inhibitor also of the WNV NS2B-NS3 protease activity with an IC_{50} value of 11.3 μM. Within the SPECS library, compound **7** exhibited comparable inhibitory potency against both ZIKV and WNV NS2B-NS3 proteases. Interestingly, compound **4** (Nilotinib) exhibited almost fourfold greater potency against WNV NS2B-NS3 with respect to ZIKV NS2B-NS3. By contrast, SPECS compound ^{16} showed a comparable potency of inhibition against ZIKV and WNV NS2B-NS3 proteases (Table 1). Finally, it is worth noting that although the IC_{50} values of other tested compounds exceeded the highest concentration tested (100 μM), partial inhibition was observed for some compounds, as indicated by residual enzymatic activity measured at this concentration, thereby supporting the effectiveness of the *in silico* selection.

2.2.2. Evaluation of compounds on ZIKV and WNV replication

Compounds that showed promising inhibitory activity against both ZIKV and WNV NS2B-NS3 proteases activity were further investigated for their ability to inhibit viral replication in cell culture in VERO E6-GFP and HuH-7, respectively (Table 2). Firstly, compounds were tested on ZIKV replication using Remdesivir as a validated positive control [38]. Among the four compounds active on ZIKV protease, compounds **3** (Nelfinavir) and **4** (Nilotinib) significantly inhibited ZIKV replication in a dose-dependent manner. Both compounds **3** and **4** showed a 100% inhibition of viral replication at a concentration of 10 μM with no cytotoxicity, with EC_{50} values of 1.79 μM and 2.09 μM, respectively, and a selectivity index (SI) > 10 (Fig. 6, panel a). In contrast, compounds **7** and **16** were inactive even at the highest concentrations tested.

The same four selected compounds were also tested for their ability to inhibit WNV replication in cell-based assays at 24 hpi using RT-qPCR (Fig. 6, panel b). Compounds **3** and **4** exhibited a strong inhibition of WNV replication, producing marked reductions in viral genome copy numbers even at low concentrations. Compound **3** achieved a 3-log10 reduction in viral genome copy numbers at 30 μM and a 2-log10 reduction at 10 μM, showing an EC_{50} value of 3.0 μM. Importantly, compound **3** exhibited moderate cytotoxicity at approximately 31 μM, yielding a SI of 10. Similarly, compound **4** displayed an almost 2-log10 decrease in viral copy number at 10 μM, which decreased to 1-log10,

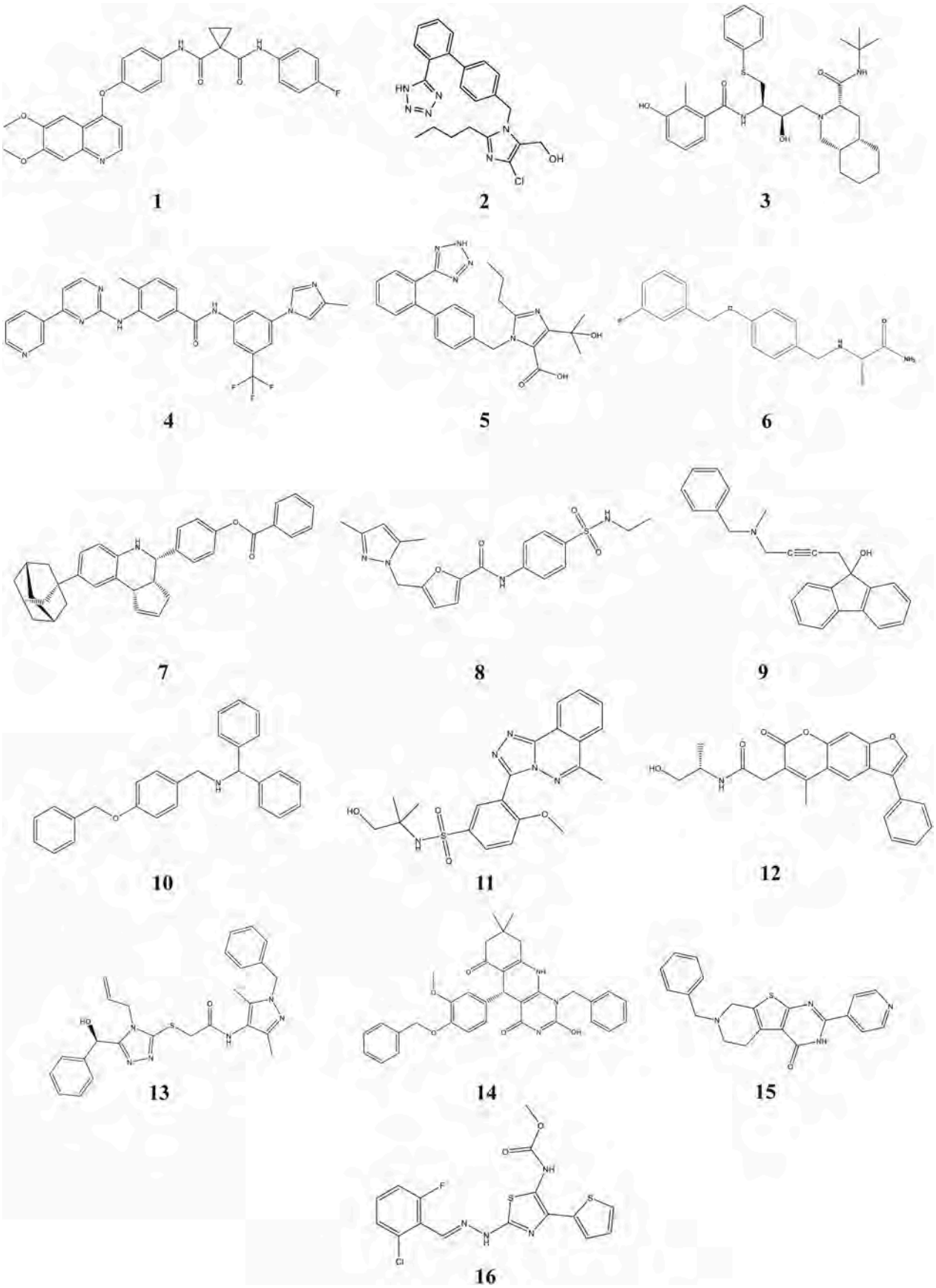

Fig. 5. 2D representation of the 16 virtual hits selected for biochemical assays.

Table 1
Inhibitory activity of the compounds against ZIKV and WNV NS2B–NS3 proteases (IC_{50} values).

CP	Name/ID	NS2B-NS3 protease	
		ZIKV [a]IC_{50} (μM)	WNV [b]IC_{50} (μM)
1	Cabozantinib	>100 (58%)[c]	>100 (52%)
2	Losartan	>100 (92%)[c]	>100 (52%)
3	Nelfinavir	13.5 ± 1.5	11.3 ± 0.65
4	Nilotinib	86 ± 2.78	23.29 ± 0.73
5	Olmesartan	>100 (90%)[c]	>100 (100%)[c]
6	Safinamide	>100 (88%)[c]	>100 (59%)[c]
7	AH-487/13431101	21 ± 1.64	13.2 ± 1.96
8	AK-968/15610123	>100 (80%)[c]	>100 (97%)[c]
9	AN-212/13751224	>100 (63%)[c]	>100 (98%)[c]
10	AN-465/41988204	>100 (82%)[c]	>100 (53%)[c]
11	AO-022/43452798	>100 (82%)[c]	>100 (57%)[c]
12	AO-022/43453921	>100 (72%)[c]	>100 (100%)[c]
13	AO-080/42576167	>100 (75%)[c]	>100 (100%)[c]
14	AP-906/41648836	>100 (57%)[c]	>100 (100%)[c]
15	AR-434/42807203	>100 (98%)[c]	>100 (100%)[c]
16	AS-871/43348421	29 ± 1.4	33 ± 1.57
Aprotinin		0.5 ± 0.1	2.3 ± 0.6
Temoporfin		4.67 ± 1.59	3.67 ± 0.71

Values are expressed as means ± SD of at least two independent experiments.
[a] Compound concentration required to inhibit the ZIKV NS2B-NS3 protease activity by 50%.
[b] Compound concentration required to inhibit the WNV NS2B-NS3 protease activity by 50%.
[c] Percentage of residual enzymatic activity at 100 μM.

showing an EC_{50} value of 2.7 μM.

Differently from what observed for ZIKV replication, compounds **7** and **16** were able to inhibit WNV replication, with a reduction of approximately 1-log10 in viral genome copy numbers at 30 μM, with EC_{50} values of 6.6 μM and 15.1 μM, for **7** and **16**, respectively, and SIs of **13** and **5**, respectively.

The different behavior observed for tested compounds against ZIKV and WNV may reflect differences in the experimental systems and will be the object of further investigation.

Furthermore, the differences between biochemical and cellular potencies are not uncommon for compounds with complex mechanisms of action, particularly when cellular accumulation and host-target modulation may contribute to the overall antiviral effect. Although the selectivity indices observed for the best compounds, **3** and **4**, indicate measurable antiviral selectivity, further optimization will be required to improve the therapeutic window and better define the relative contribution of viral and host-directed mechanisms.

2.2.3. *Kinetics of inhibition of ZIKV and WNV NS2B-NS3 proteases by compound **3***

Compound **3** (Nelfinavir) exhibited the highest inhibitory activity against both ZIKV and WNV NS2B-NS3 proteases in the biochemical assay and in suppressing their viral replication in cell-based experiments. Hence, we investigated its mode of action by performing enzyme inhibition kinetics on both enzymes, varying substrate concentrations in the presence of increasing concentrations of the compound (Fig. 7). Michaelis-Menten analysis showed a compound concentration-dependent decrease in the maximum reaction velocity (V_{max}), while the K_m remained constant (Fig. S6). Consistently, data analyzed using the Lineweaver-Burk plot of reciprocal reaction velocity versus reciprocal substrate concentration show an intersection of the lines at the negative X-axis, indicating a non-competitive inhibition mechanism. Indeed, as expected, the inhibition constants (K_i), measured in the kinetics of inhibition, were consistent with the IC_{50} values for both ZIKV and WNV NS2B-NS3 protease [39].

2.2.4. *Compound **3** binding to ZIKV and WNV NS2B-NS3 proteases*

To further characterize the binding of compound **3** to both ZIKV and WNV NS2B-NS3 proteases, a differential scanning fluorimetry (DSF) assay was performed to evaluate ligand-induced changes in protein thermal stability. Results showed that compound **3** was able to increase the ZIKV NS2B-NS3 protease melting temperature (T_m) from 44 °C to 46 °C, corresponding to a positive thermal shift (ΔT_m) of approximately +2 °C (Fig. 8, panel a). This increase in melting temperature indicates ligand-induced stabilization of the protease, supporting the hypothesis of the formation of a compound-protease complex. In contrast, when WNV NS2B-NS3 protease was incubated in the presence of compound **3** (Fig. 8, panel b), a negative thermal shift (ΔT_m) of 0.5 °C was observed, suggesting a slight ligand-induced destabilization of the protease, still consistent with an interaction between compound **3** and the protease. In both cases, compound **3** proved to have a role in modulating the conformational dynamics of the protease, with functional consequences on its catalytic activity, in agreement with the inhibitory activity observed in enzymatic assays. Aprotinin was included as a reference control, determining a thermal shift of 7.5 and 2 °C when incubated in presence of ZIKV and WNV NS2B-NS3 proteases, respectively, confirming the suitability of the assay conditions.

Considering all the data obtained, it can be noted that EC_{50} values for compound **3** were lower than the IC_{50} observed against the NS2B-NS3 protease, indicating that additional factors may require further investigation. Indeed, Nelfinavir mesylate is a well-known HIV-1 protease blocker that has demonstrated broad-spectrum antiviral activity extending well beyond its primary indication. Notably, it was confirmed to inhibit herpes simplex virus 1 (HSV1), and the replication of several other herpesviruses by interfering directly or indirectly with the later steps of virus formation, such as glycoprotein maturation or virion release, other than functioning in herpesviruses protease [40]. It is also active on the Chikungunya virus (CHIKV) [41]. More recently, its antiviral potential has been extended to SARS-CoV-2, with EC_{50} values of approximately 1.9-2.9 μM against wild-type virus and major variants of concern, including Delta and Omicron, in both Vero E6 and Calu-3 cells. It has been demonstrated that this activity involves host cell pathways, including inhibition of cyclophilin A, proteasome-mediated unfolded protein response, suppression of PI3K/Akt signaling, and modulation of innate immune responses [42]. Regarding the flavivirus infections, it

Table 2
Antiviral activity of selected compounds against ZIKV and WNV replication.

CP	ZIKV VeroE6-GFP 96h [a]EC_{50} (μM)	VeroE6-GFP 96h [b]CC_{50} (μM)	ZIKV Selectivity Index (SI)	WNV HuH-7 24h [a]EC_{50} (μM)	HuH-7 24h [b]CC_{50} (μM)	WNV SI
3	1.79 ± 0.01	24.13 ± 0.55	13.4	3.01 ± 1.25	31.66 ± 1.12	10.5
4	2.09 ± 1.02	33.01 ± 3.4	15.8	2.70 ± 1.11	16.48 ± 1.23	6.1
7	>100	>100	-	6.69 ± 1.93	87.87 ± 13.13	13.13
16	>100	>100	-	15.12 ± 1.09	80.32 ± 8.38	5.3
Remdesivir	1.94 ± 0.63	33.06 ± 6.9	17.0	0.24 ± 0.003	64.28 ± 1.77	267.8

Results report the mean and standard deviation of at least two independent biological experiments.
[c] Selectivity index: CC_{50}/EC_{50} ratio.
[a] Compound concentration required to reduce by 50% ZIKV or WNV cytopathic effect.
[b] Compound concentration required to reduce by 50% Vero E6-GFP or HuH-7 viability.

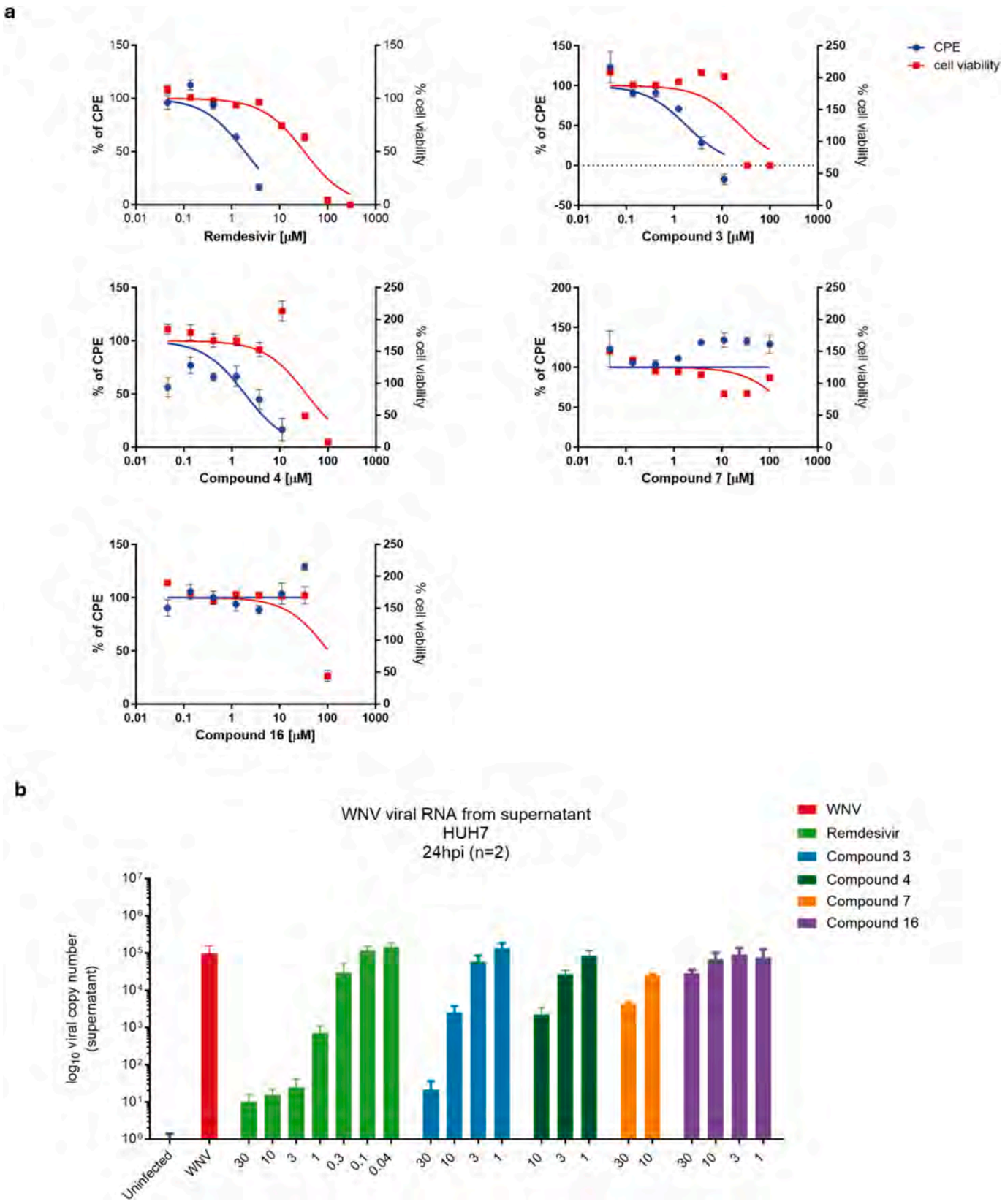

Fig. 6. Dose-response curve of the selected compounds against ZIKV and WNV replication. a) Evaluation of compounds **3**, **4**, **7**, **16** together with the positive control Remdesivir, against ZIKV replication in Vero E6-GFP cells. Antiviral efficacy was assessed at 96 h post-infection (hpi), and EC_{50} values were calculated from dose-response curves. b) Evaluation of compounds against WNV replication: untreated (red), Remdesivir (green), **3** (teal), **4** (dark green), **7** (orange), **16** (purple). The WNV RNA was measured in the supernatant by RT-qPCR at 24h post-infection, and dose-response curves are plotted as log10 viral copy number.

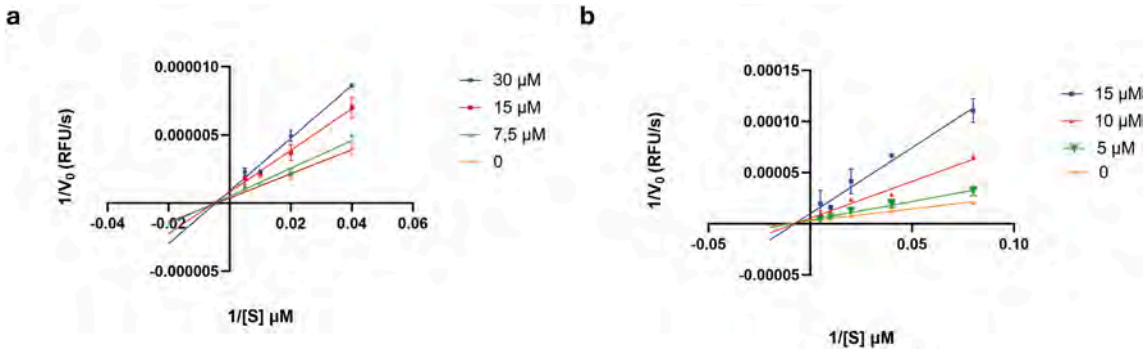

Fig. 7. Lineweaver-Burk plots of compound **3** (Nelfinavir) on ZIKV and WNV NS2B-NS3 protease. a) ZIKV NS2B-NS3 protease inhibition kinetic was measured at 30 (blue), 15 (red), 7.5 (green), and 0 (orange) µM of compound **3** in the presence of 200, 100, 50, and 25 µM of peptide substrate. b) WNV NS2B-NS3 protease inhibition kinetic was measured at 15 (blue), 10 (red), 5 (green), and 0 (orange) µM of compound **3**, with the same peptide substrate concentration used for ZIKV NS2B-NS3 protease.

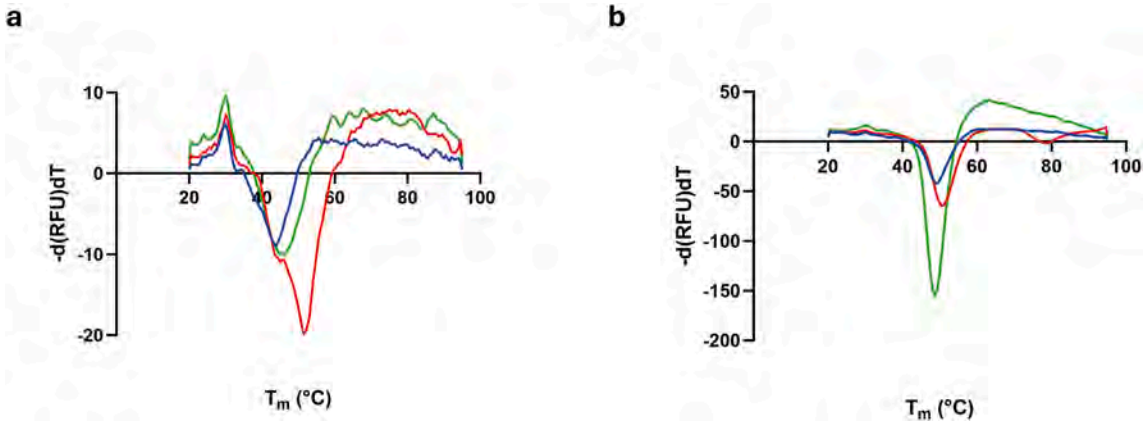

Fig. 8. Differential scanning fluorimetry of NS2B-NS3 protease. a) DSF of ZIKV NS2B-NS3 protease performed on the protein alone (blue) or on the protein incubated with Aprotinin (red) or with compound **3** (green). b) DSF of WNV NS2B-NS3 protease performed on the protein alone (blue) or on the protein incubated with Aprotinin (red) or with compound **3** (green).

was mentioned that Nelfinavir may act on flavivirus NS4B [43]. In a following article, Nelfinavir showed activity against DENV2 with an EC_{50} of 3.5 ± 0.4 µM and was proposed as a starting point for the development of broad-spectrum protease inhibitors targeting the viral NS2B-NS3 complex. However, its activity was predicted on the catalytic site of NS3, by docking simulations [41]. Conversely, we demonstrated that Nelfinavir is able to inhibit NS3 by binding an allosteric site. Overall, this study adds a further piece to this extremely interesting and complex mosaic of antiviral activity.

Therefore, allosteric inhibition of NS2B-$NS3^{pro}$ should be considered a plausible and experimentally supported mechanism contributing to the antiviral activity of compound **3**, rather than the sole determinant of its cellular effect.

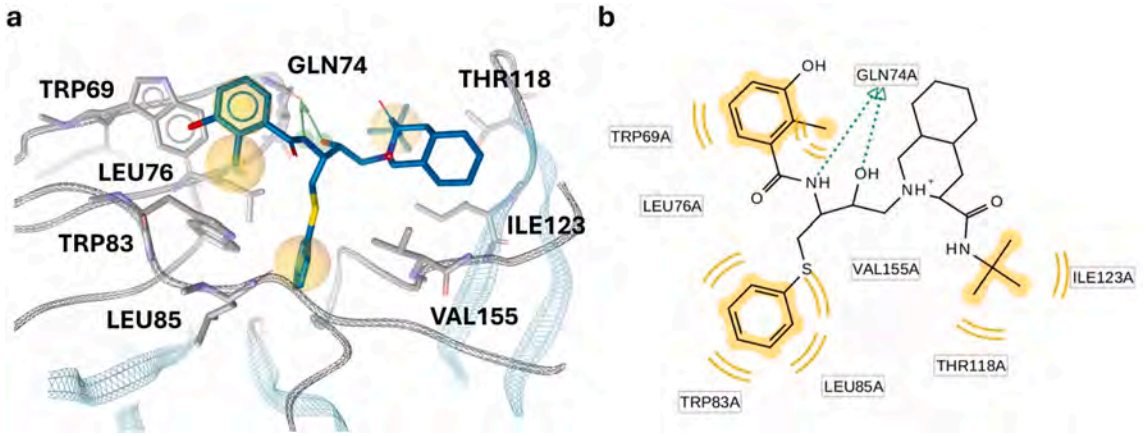

Fig. 9. Predicted binding mode of compound **3** within the proposed allosteric pocket of ZIKV NS2B-NS3 protease. a) 3D representation of the docked complex, highlighting the residues predicted to interact with compound **3**. Residue L76, located in the central region of the putative allosteric cavity, was selected for site-directed mutagenesis based on its predicted contribution to ligand recognition. b) 2D ligand-protein interaction diagram showing the main hydrophobic contacts (in yellow) and HB interactions (green arrows) stabilizing compound **3** within the allosteric binding pocket.

*2.2.5. Experimental and computational investigation of the proposed allosteric binding site of compound **3***

To further investigate the molecular basis of compound **3** inhibition and to provide experimental support for the proposed allosteric binding mode, we used the ZIKV NS2B-NS3 protease model previously described in the computational workflow as the structural basis for molecular docking studies. Analysis of the predicted binding pose of compound **3** and evaluation of the protein-ligand pharmacophoric features identified residue L76 as a potential hotspot within the proposed allosteric cavity (Fig. 9, panel a). Indeed, L76 occupies a central position within the hydrophobic binding pocket and contributes to the stabilization of the ligand through hydrophobic contacts with the aromatic core of compound **3** (Fig. 9, panel b). Based on these observations, residue L76 was selected for site-directed mutagenesis in the ZIKV NS2B-NS3 protease. In parallel, the residue at the corresponding position in the WNV NS2B-NS3 protease (R76) was also substituted with alanine to determine whether this structurally conserved region contributes to compound recognition in the related flaviviral protease.

The mutant proteases were successfully expressed and purified to assess, in terms of catalytic efficiency, the effect of the mutations compared to the wild-type (WT) enzymes. As shown in Table 3, the ZIKV L76A mutant exhibited decreased substrate affinity (K_M) along with a 28 fold reduction in catalytic turnover (K_{cat}), resulting in a significant decrease in catalytic efficiency (K_{cat}/K_M), compared to the ZIKV WT protease. This suggests a fundamental role of the L76 residue in maintaining the structural integrity of the enzyme and, consequently, its associated catalytic activity. On the contrary, the R76A mutation in WNV protease resulted in an approximately 3-fold increase in catalytic turnover (K_{cat}), accompanied by a marked increase in catalytic efficiency (K_{cat}/K_M) coupled with reduced substrate affinity (K_M). These kinetic data suggest that the mutation can induce stabilization of the enzyme in a more catalytically productive conformation, but less favorable for substrate binding (Fig. S7). Compound **3** inhibition was evaluated for both ZIKV and WNV mutants (Table 4). ZIKV L76A mutant led to a complete loss of inhibitory activity at the highest tested concentration, supporting the involvement of this residue in the compound **3** binding mode. In contrast, less pronounced change in compound **3** inhibitory activity was observed for the WNV R76A variant when compared to the WT. Temoporfin, used as a reference control in the assay, exhibited a 2-fold decrease in inhibitory potency in both ZIKV and WNV mutants compared to the WT enzymes, likely due to protein rearrangements. Summarizing, these data indicate that, although the ZIKV L76A mutation is associated with reduced catalytic efficiency, it does not impair enzymatic function or compromise assay reliability, supporting the specificity of the observed resistance of compound **3** toward the mutant. On the other hand, the moderate loss of compound **3** inhibitory activity observed for the WNV R76A mutation can be attributed to protein conformational rearrangements, while the compound still maintains stabilizing interactions within the binding pocket.

To further elucidate the effects of the selected mutation on the ZIKV NS2B-NS3 protease, MDs were performed on both the WT and L76A mutant enzymes in complex with compound **3**. MDs revealed a distinct difference in the ligand dynamics between the two systems. Although the overall protein structure remained stable, as shown by similar P-RMSD profiles (Fig. 10, panel a), the ligand exhibited much greater conformational fluctuations in the L76A mutant than in the WT complexes (Fig. 10, panel b). Notably, the mutant systems showed a gradual increase in L-RMSD, surpassing 10 Å, whereas the ligand remained more stable in the WT. Additionally, ligand atom RMSF (L-RMSF) analysis indicated significantly increased fluctuations throughout the molecular scaffold in the L76A mutant, especially at the molecule's terminal regions, reflecting a considerable loss of conformational restraint due to the L76 mutation (Fig. 10, panel c).

Table 3
Kinetic parameters of ZIKV and WNV wildtype and mutant enzymes.

Construct	K_M (μM)	K_{cat} (s^{-1})	K_{cat}/K_M ($M^{-1}s^{-1}$)
ZIKV WT	143.53 ± 19.35	0.0359 ± 0.0036	242.22 ± 22.53
ZIKV L76A	195.35 ± 44.76	0.0013 ± 0.0001	6.66 ± 1.02
WNV WT	129.5 ± 7.23	0.0171 ± 0.001	132.74 ± 13.99
WNV R76A	232.23 ± 3.86	0.0593 ± 0.0061	255.21 ± 23.34

To quantitatively evaluate the energetic profile, MM/GBSA calculations were performed on representative frames extracted from MD trajectories (Table 5).

Results showed that the WT complexes exhibit a more favorable binding free-energy profile than the L76A mutants. This energetic penalty was primarily associated with less lipophilic and van der Waals contributions, suggesting that residue L76 contributes predominantly to the hydrophobic stabilization of compound **3** within the proposed allosteric cavity. Moreover, the higher SD and coefficient of variation (CV) values observed for the mutant trajectories indicate increased energetic heterogeneity and reduced stability of the protein-ligand complex. Also, the interquartile ranges (Q25-Q75) of the MM/GBSA distributions move toward less favorable binding energies in the mutant systems. Next, to understand this effect, we examined whether ligand-residue contacts persisted throughout the MDs (Table S3). The L76A mutation significantly reduced contact occupancy with hydrophobic residues, including W69, W83, and I123, while interactions with V155 remained largely intact due to complex loss of stability. Overall, these findings suggest that the L76A mutation mainly impairs ligand recognition by disrupting the local hydrophobic environment, while maintaining the protease's overall structural integrity.

The obtained computational and biochemical data collectively provides a coherent framework supporting the proposed allosteric mechanism of inhibition.

3. Conclusion

In this study, we implemented an integrated computer-aided drug design (CADD) workflow to identify novel inhibitors of the ZIKV NS2B-NS3 protease, a key enzyme in the flavivirus replication cycle, and a validated antiviral target. By combining MD simulations, LigandScout representative pharmacophore models, pharmacophore-based virtual screening, and MRC docking experiments, we efficiently explored the protease's noncanonical binding regions and prioritized a targeted set of candidates for experimental evaluation.

Biochemical assays identified several NS2B-NS3 flavivirus protease inhibitors, with Nelfinavir proving to be the most potent inhibitor against both ZIKV and WNV enzymes. Cell-based assays further confirmed the antiviral activity of selected compounds, with Nelfinavir and Nilotinib displaying low-micromolar activity against viral replication and favorable SI.

Enzyme kinetics indicated a noncompetitive inhibition mechanism for Nelfinavir, supporting the proposed interaction with an allosteric site on the protease. Importantly, the observed cross-inhibition against ZIKV and WNV proteases demonstrates the potential of targeting conserved allosteric regions for the development of potential broad-spectrum flavivirus inhibitors. The identification of approved drugs as flavivirus replication inhibitors also reinforces the feasibility of drug repositioning strategies to accelerate the development of antiviral therapies.

Overall, this work demonstrates the effectiveness of combining several structure-based approaches with VS and experimental validation for the discovery of allosteric inhibitors of complex viral targets. The identified compounds provide promising starting points for further optimization and mechanistic studies aimed at developing new therapeutic options against ZIKV, WNV, and other related flaviviruses.

In particular, the novelty of the present study resides in: (i) the development and application of an integrated CADD workflow combining MD-derived pharmacophore modeling, virtual screening, docking, and experimental validation; (ii) the identification and experimental validation of a putative allosteric binding mode for Nelfinavir;

Table 4
Inhibitory activity of compound 3 against ZIKV and WNV WT and mutant enzymes.

CP	ZIKV NS2B -NS3 WT IC_{50} (μM)	ZIKV NS2B -NS3 L76A IC_{50} (μM)	Fold change respect to WT	WNV NS2B -NS3 WT IC_{50} (μM)	WNV NS2B -NS3 R76A IC_{50} (μM)	Fold change respect to WT
3	9.73 ± 1.64	>100	>10	9.18 ± 1.45	28.6 ± 1.68	3.12
Temoporfin	4.67 ± 1.59	9.55 ± 0.27	2.05	3.67 ± 0.71	7.63 ± 0.94	2.08

(iii) the demonstration of dual activity against ZIKV and WNV through the targeting of the allosteric region of the NS2B-NS3^{pro}, supporting the potential broader applicability of this site across flavivirus proteases, which will require further validation in additional members of the *Flaviviridae* family.

4. Experimental section

Computational Details. We used a series of CADD and bioinformatics tools to perform data analysis, create models for virtual screening, perform virtual screening, and prioritize virtual hits to identify the most promising compounds for acquisition and biological testing.

Target and database optimization. The crystal structure of the ZIKV NS2B-NS3 protease (PDB ID 7M1V [26,44]) was retrieved as shown in the KNIME workflow and optimized using the Protein Preparation Wizard [45] to assign bond orders, add hydrogen atoms, adjust disulfide bonds, and assign the protonation states of residues at pH 7.4. The N- and C-termini were capped to avoid terminal charges. All crystallographic water molecules were removed. The complex was then subjected to 10,000 iterations of energy minimization using the Polak-Ribiere conjugate gradient (PRCG) algorithm in the MacroModel tool, with the OPLS2005 force field [46]. The FDA and SPECS libraries were obtained from DrugBank (www.drugbank.com) [47] and SPECS (www.specs.net) databases. The set of active and inactive molecules was downloaded from ChEMBL (www.ebi.ac.uk/chembl/) and used to generate LigandScout libraries for pharmacophore validation. All compounds were prepared using the LigPrep tool [48]. Hydrogen atoms were added, salts were removed, and ionization states were calculated using Epik at pH 7.4 ± 0.0. Each structure was subjected to 10,000 iterations of energy minimization using the Polak-Ribiere conjugate gradient (PRCG) algorithm in the MacroModel tool with the OPLS2005 force field [46].

Conventional Molecular Dynamics. Conventional molecular dynamics (cMD) simulations of NSC86314-ZIKV NS2B-NS3^{pro}, WT, and ZIKV L76A complexes were carried out using the Desmond package [49]. The optimized systems were solvated in an orthorhombic periodic box with a 12 Å buffer between the solute and the box edges. The TIP3P explicit water model [50] was used, and the system charge was neutralized with Na^+ counterions. Production runs were performed under NPT conditions using a Langevin thermostat and barostat, each with a relaxation time constant of 5.0 ps, to keep the temperature at 300 K and the pressure at 1.01325 bar. Short-range nonbonded interactions were truncated at 9.0 Å, and long-range electrostatic interactions were handled using the Particle Mesh Ewald (PME) method [51]. Initial atomic velocities were assigned based on a Maxwell–Boltzmann distribution at 300 K, using a random *seed*. Integration was performed using a multi-timestep RESPA scheme, employing 2.0 fs time steps for bonded and short-range non-bonded interactions, and 6.0 fs for long-range interactions. Regarding the NSC86314-ZIKV NS2B-NS3^{pro} complex, two independent simulations, each lasting 1 μs, were performed. For WT and ZIKV L76A complexes, two independent simulations, each lasting 400ns, were run. All MD trajectories (available upon request) were analyzed using Maestro (Schrödinger Release 2024-1) and using Visual Molecular Dynamics (VMD) [52]. For each complex, structural stability was evaluated through RMSD analysis calculated on the protein (*P*) backbone and ligand (*L*) heavy atoms; clustering of the MD trajectories was performed using the Trajectory Frame Clustering Panel to identify the most representative conformational state (cluster c0). Frames used for RMSD calculation were selected from the trajectory at 10-frame intervals. All frames were superimposed prior to calculating the RMSD. Consequently, the RMSD matrix was used in the affinity propagation clustering method [53]. Binding free-energy calculations were performed on representative frames extracted from the MDs of all systems using the thermal_mmgbsa.py workflow implemented in Schrödinger Suite 2026-1 (Schrödinger LLC, New York, NY, USA). Frames were sampled every 10 simulation frames, yielding 101 representative conformations for each trajectory. MM/GBSA calculations were carried out using Prime MM/GBSA with the VSGB 2.1 implicit solvent model and the OPLS force field under the local minimization protocol (REAL_MIN). For each trajectory, binding free energies (ΔG_bind) and their lipophilic (ΔG_Lipo) and van der Waals (ΔG_vdW) contributions were calculated. Mean values, standard deviations (SD), coefficients of variation (CV), and interquartile ranges (Q25-Q75) were subsequently determined to characterize the energetic distributions.

Pharmacophore models generation and PBVS. LigandScout 4.5 Expert extensions for the KNIME Analytics platform version 4.7.1 [25,54] was used to generate both Static (minimized X-ray structure) and Representative Pharmacophore Models (RPMs) using LigandScout 4.5 Expert direct approach [55] and LigandScout MD analysis tools (additional SD material 02_PBVS_MCR_data.xls). Feature constraints are left as the default option. The RPMs were generated using the "MD pharmacophore creator" node from Inte:Ligand LigandScout Expert Extensions for KNIME. Exclusion volumes (XVOLs) were automatically calculated by LigandScout and added to each model. We chose to discard the molecules of water added for the MD simulations before the pharmacophore chemical-feature interaction analyses. Next, the Static-hypo, RPM1-hypo, and RPM2-hypo pharmacophore models were validated using a set of active/inactive libraries. Compounds with documented IC_{50} activity against ZIKV were retrieved from ChEMBL (https://www.ebi.ac.uk/chembl/explore/target/CHEMBL4523954) and divided into active (606, $IC_{50} < 50$ μM) and inactive (2343, $IC_{50} > 100$ μM) groups, after duplicates removal. All molecules were converted into library files (*.ldb*) for virtual screening using the LigandScout PBVS command-line tool, idbgen, with default settings. Conformers were calculated using iCon from LigandScout with the 'best' option, with a maximum of 200 conformations processed for each molecule.

Multiple Receptor Conformation (MRC) docking studies. The combined set of 1539 hit compounds resulting from the three PBVS (additional SD material 02_PBVS_MCR_data.xlsx) were subjected to molecular docking studies by means of Glide [56]. To prioritize hit ranking, an MRC docking study was applied, considering five conformations: *conf_0*, representing the starting-minimized NSC86314-ZIKV NS2B-NS3 protease complex; *conf_1*, reflecting the representative frame (578) of the RPM1; *conf_2*, reflecting the representative frame (833) of the RPM2; *conf_3* and *conf_4*, reflecting the two independent representative MD clusters (c0). For all conformations, a grid box of 12x12x12 Å^3 centered on the ligand was generated. The Glide ligand flexible algorithm with the standard precision (SP) protocol was used. For the final selection, the G-score profile of each compound in each single run was observed, and then an overall average was calculated to highlight the best ranking. Promising compounds were selected based on a threshold of −5.5 kcal/mol Average MCR G-score (marked with a star in the additional SD 02_PBVS_MCR_data.xlsx). However, docking scores were used exclusively as relative ranking metrics within the virtual screening

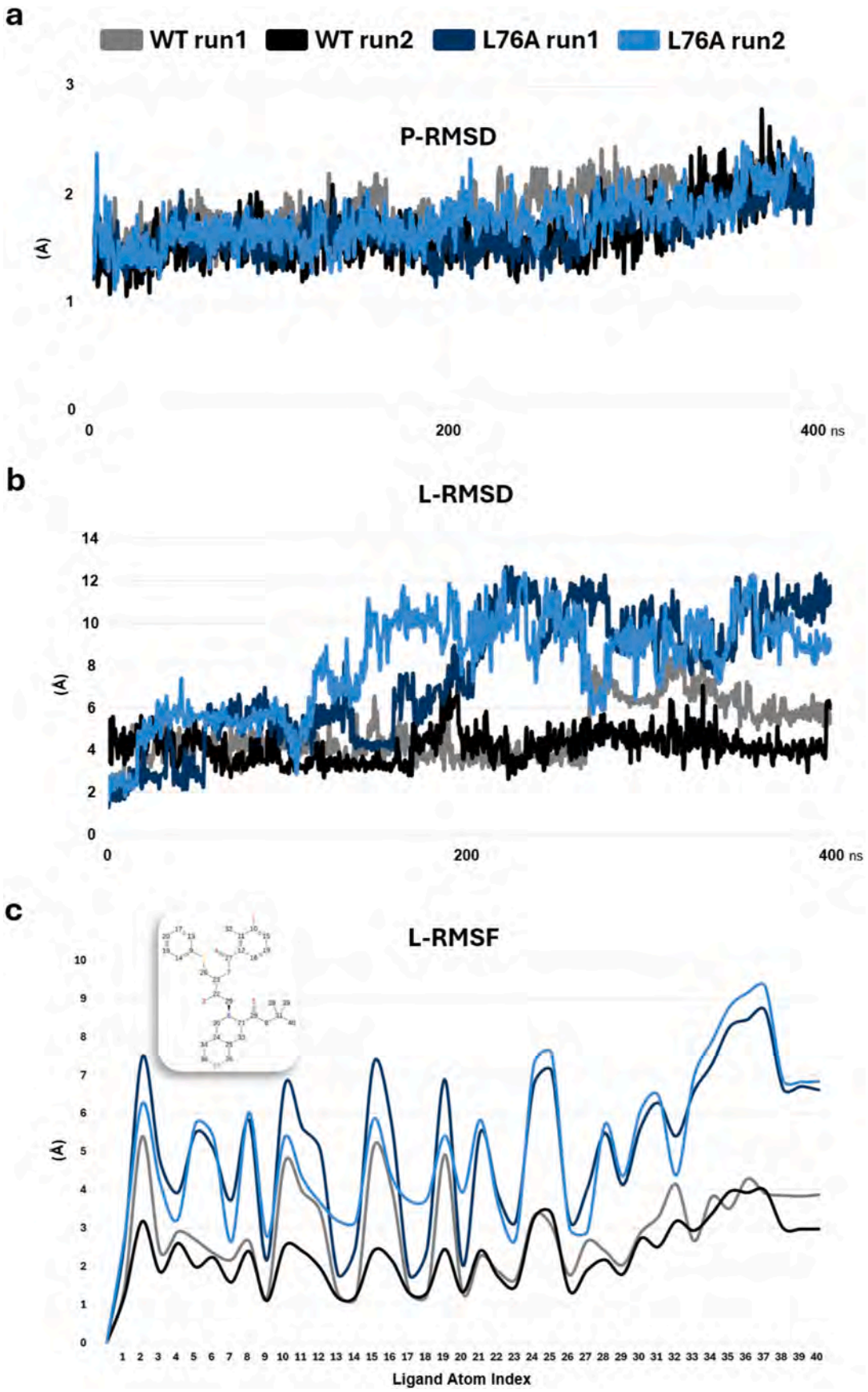

Fig. 10. MD analysis of compound **3** binding to ZIKV NS2B-NS3 protease WT and L76A complexes. a) P-RMSD and b) L-RMSD profiles from two independent MD runs. c) Ligand atom RMSF profiles showing the positional fluctuations of compound **3** atoms throughout the simulations.

Table 5
MM/GBSA binding free energy analysis of compound **3** in complex with WT and L76A mutant ZIKV NS2B-NS3^{pro} calculated from the MDs. The table reports the mean binding free energy (ΔG_bind), the corresponding lipophilic (ΔG_Lipo) and van der Waals (ΔG_vdW) contributions. Standard deviation (SD), coefficient of variation (CV), and the percentiles are reported (Q25; Q75). Values are reported as mean ± standard deviation over the analyzed MD frames.

MD	Mean ΔG[b]	Mean ΔG LIPO[b]	Mean ΔG vdW[b]	SD	CV (%)	Q25[a]	Q75[a]
WT run1	−55.44	−23.5	−49.2	6.13	11.06	−59.29	−51.65
WT run2	−55.26	−23.9	−48.7	7.58	13.72	−60.12	−50.00
L76A run1	−53.70	−21.6	−44.9	8.68	16.17	−58.97	−46.87
L76A run2	−49.75	−20.4	−44.1	8.12	16.31	−55.33	−43.57

[a] Q25 and Q75 define the interquartile range containing the central 50% of the sampled MM/GBSA values and provide a measure of the robustness and variability of the binding-energy distributions.
[b] Values expressed in kcal/mol.

workflow and should not be interpreted as experimental measures of binding affinity.

Computational and Software Resources. The Schrödinger software suite (Release 2024-1) was employed through Maestro, its graphical user interface (GUI). Simulations were carried out on NVIDIA RTX A5500 GPUs using the GPU-accelerated Desmond engine on a Linux-based workstation (Dell Precision 7960 Tower). In addition, the computational infrastructure provided access to more than 100 CPU cores, enabling efficient parallelization of molecular modeling and data processing tasks. The KNIME Analytics Platform was used to design workflows (*.wkf*), manage datasets, and process computational results. LigandScout 4.5 Expert Extensions for KNIME were used to develop 3D pharmacophores from X-ray structures and to analyze interaction frequencies from MD simulations. Images of the proteins were rendered using Maestro GUI Suite 2024-4 and Adobe Illustrator (Adobe Systems, San Jose, CA, USA). Images of the pharmacophores and ligands with pharmacophores were rendered using LigandScout 4.5 Expert.

Supplementary Data also includes the dataset of ZIKV PDB structures, the PBVS-MCR screening results, and pdb obtained after the two independent MD runs of the protein-ligand complex.

Purchased molecules. The compounds used in this study were purchased from SPECS and Biosynth suppliers. The reported purities of these compounds were ≥95%, as provided by the suppliers. HPLC analyses were performed for the key active compounds **3**, **4**, **7**, and **16**.

The analyses were carried out on an Agilent 1260 HPLC system using a Kinetex C18 column (250 mm × 4.6 mm, 5 μm particle size) at a flow rate of 1.0 mL/min. For compound **3**, the mobile phase consisted of water and acetonitrile employing a linear gradient from 55% to 80% acetonitrile over 5 min. For compound **4**, the same mobile phase was employed, with the acetonitrile content increasing from 55% to 90% over 2 min. For both compounds, detection was obtained at 250 nm via a Diode Array Detector (DAD). For compound **7**, the mobile phase consisted of water (5%) and acetonitrile (95%), and detection occurred at 250 nm. Finally, for compound **16**, the mobile phase consisted of water (40%) and acetonitrile (60%), and detection was performed at 280 nm. The corresponding chromatograms are provided as Supporting Material (Figs. S8–S11), and confirmed that the purity of each compound was consistent with the supplier's specifications.

ZIKV NS2B-NS3 protease construct. A catalytically active construct of ZIKV NS2B-NS3 was obtained connecting with a G4SG4 linker, the C-terminal β-hairpin of NS2B (4354- 4494 from KU321639.1 zika sequence) with the active site of NS3 (4612- 5193 from KU321639.1 zika sequence). Sequence was optimized for *E. coli* expression with vector builder Version 2.1.409 enzyme sites: *Bam*HI [GGATCC]; NdeI [CATATG] were excluded. Sequence was inserted into a pET15b under NdeI and *Bam*HI sites, with His-tag in N-term (genscript).

Site-directed mutagenesis of ZIKV and WNV NS2B-NS3 proteases. Amino acid substitutions were introduced into the plasmids encoding ZIKV and WNV NS2B-NS3 proteases, using a QuikChange mutagenesis kit (Agilent Technologies Inc.) following the manufacturer's instructions.

ZIKV and WNV NS2B-NS3 expression and purification. ZIKV and WNV NS2B-NS3, wild types and mutants, were expressed in *E. coli*. Briefly, *E. coli* BL21(DE3) cells were transformed with a single plasmid encoding for either ZIKV or WNV (VectorBuilder ID:VB230801-1377xta) NS2B and-NS3 protease domain. Overnight seed cultures were grown at 37 °C in LB medium supplemented with 150 μg/mL ampicillin for ZIKV and 50 μg/mL kanamycin for WNV proteases. The seed cultures were then used to inoculate 4 L of LB medium for large-scale recombinant protein expression. Cells grew at 37 °C until reaching an OD_{600} of ~0.6, followed by induction with 0.5 mM isopropyl-β-D-1-thiogalactopyranoside (IPTG). ZIKV NS2B-NS3 was expressed by incubating the culture for 4 h at 37 °C whereas WNV NS2B-NS3 by incubating the culture for 16 h at 18 °C. Finally, cells were harvested by centrifugation at 4000 ×*g* and stored at −80 °C until further use. ZIKV NS2B-NS3 bacterial pellets were re-suspended in 50 mM Tris-HCl pH 8.5, 500 mM NaCl, 20 mM Imidazole, 5% Glycerol, 5 mM β-mercapto-ethanol (buffer A) with 1 mg/ml lysozyme and 1 mM PMSF. Cells were disrupted by sonication for 10 min (1″ on, 1" off) and the soluble fraction collected by centrifugation (16,000×*g*) for 1h at 4 ∘C. The soluble fraction was loaded on 5 ml Ni^{21}-NTA affinity column (Cytiva). The column was washed with 25 ml of buffer A with 40 mM imidazole, and the protease fractions were eluted with buffer A containing 500 mM imidazole. The eluted protein was dialyzed in presence of Buffer A in absence of imidazole for 4h at 250 rpm, replacing buffer A every 2 h. The dialyzed protein was analyzed for purity by SDS-PAGE and stored at −80 °C.

Differently, WNV NS2B-NS3 bacterial pellets were re-suspended in 50 mM Tris-HCl pH 8.5, 300 mM NaCl, 10 mM Imidazole, 5% Glycerol, 5 mM β-mercapto-ethanol (buffer A) with 0.04 mg/ml lysozyme and cOmplete EDTA-free Protease Inhibitor Cocktail (Roche). Cells were disrupted by sonication for 15 min and the soluble fraction collected by centrifugation (16,000×*g*) for 45 min at 4 ∘C. The soluble fraction was loaded on 5 ml Ni^{2+}-NTA affinity column (Cytiva). The column was washed with 25 ml of buffer A, and the protease fractions were eluted with buffer A containing 300 mM imidazole. The eluted protein was diluted 1:10 in buffer 50 mM Tris-HCl pH 8.5, 5% Glycerol, 5 mM β-mercapto-ethanol (Buffer B), and subsequently loaded onto a 5 mL HiTrap anion exchange column (Cytiva). The column was washed with 25 mL of Buffer B and the protein eluted using a linear NaCl gradient (0-300 mM). Fractions containing WNV NS2B-NS3 were pooled and further purified by size exclusion chromatography using Superdex 16/600 column (Cytiva). The column was equilibrated with buffer containing 50 mM Tris-HCl pH 8.5, 300 mM NaCl, 5% Glycerol (buffer C), and the protein eluted. The protein fractions were analyzed for purity by SDS-PAGE and stored at −80 °C.

Activity and inhibition assays for ZIKV and WNV NS2B-NS3 proteases. The ZIKV and WNV NS2B-NS3 protease activities were measured using fluorescent proteinase activity assay, in 384 black-well plates (PerkinElmer), using as substrate a peptide labelled with an AMC fluorophore at one end. ZIKV and WNV NS2B-NS3 were pre-incubated at 37 °C for 10 min at final concentrations of 200 nM and 250 nM, respectively, in the reaction mixture, containing 50 mM Tris pH 8.5, 10% glycerol, 0.5 mM CHAPS, and in presence of serial dilutions of inhibitors (or with 5% DMSO as a control). To initiate the reaction, 20 μM and 25 μM of Pyr-RTKR-AMC (Bachem) were added, for ZIKV and WNV proteases, respectively. The fluorescence signal generated by substrate cleavage mediated by the proteases was recorded for 30 min using Victor Nivo (PerkinElmer) at 355/435 nm. Aprotinin and Temoporfin were used as a validated positive control in the assay. The same protocol was applied for the evaluation of the activity and inhibition of ZIKV and WNV mutant enzymes, adjusting enzyme and substrate concentration to ensure sufficient enzymatic activity for the assay. The tight-binding inhibitor Temoporfin was used as a reference control when evaluating the inhibition of mutant enzymes, since the inhibitory activity of Aprotinin, which behaves as a tight-binding orthosteric inhibitor, can be influenced by the loss of catalytic efficiency of the protease variants.

Determination of the kinetic of ZIKV and WNV NS3 proteases inhibition. The kinetics of inhibition of ZIKV and WNV NS2B–NS3 protease activities were measured using fluorescent proteinase activity assay performed in black 384-well plates (PerkinElmer) with a fluorogenic peptide substrate. ZIKV and WNV NS2B–NS3 were pre-incubated at 37 °C for 10 min at a final concentration of 250 nM and 200 nM, respectively, in reaction buffer containing 50 mM Tris-HCl pH 8.5, 10% glycerol, and 0.5 mM CHAPS, in the presence of increasing concentrations of inhibitors or 5% DMSO as a negative control. Reactions were initiated by adding the substrate Pyr-RTKR-AMC (Bachem) at concentrations of 12.5, 25, 50, 100 and 200 μM. Fluorescence generated by substrate cleavage was recorded at 30 min using a Victor Nivo plate reader (PerkinElmer) with excitation/emission wavelengths of 355/435 nm. Results were plotted in a Lineweaver-Burk graph as reciprocals of reaction velocity (RFU/sec) against the reciprocals substrate (μM) in the presence of different inhibitor concentrations. The data points were plotted using GraphPad Prism (version 10.1.0) software.

Differential scanning fluorimetry assay (DSF). The DSF assay was conducted using 10 μM of ZIKV and WNV NS2B-NS3 in a reaction mix containing 50 mM Tris-HCl pH 8.5, 0.5 mM CHAPS, 5X SYPRO Orange dye. Compounds added at a final concentration of 40 μM were pre-incubated for 30 min at RT, and subsequently, reactions were started in triplicate in a 96-well clear plate with a total volume of 50 μL. The fluorescence (EXT/EM, 492 nm/610 nm) was monitored in a CFX-96 RT PCR detection system (Bio-Rad) at 0.5 °C intervals over a range of 25-95 °C using FAM as a fluorophore filter to monitor the change in the fluorescence intensity upon the denaturation of NS2B-NS3 protease. The observed fluorescence intensity of the SYPRO dye was normalized to compute the melting temperature.

Evaluation of inhibition of WNV replication in HuH-7 cells by RT-qPCR Assay. HuH-7 human hepatoma cells were cultured in Dulbecco's modified Eagle medium (DMEM, Gibco) supplemented with 10% (v/v) heat-inactivated fetal bovine serum (FBS-HI, Gibco) and 1× penicillin-streptomycin (EuroClone) at 37 °C in a presence of 5% CO_2. The WNV strain UVE/WNV/1999/US/NY 385-99 was provided by EVA and propagated in the mosquito-derived C6/36 cell line. All virus-related work was carried out in certified, high-containment Biosafety Level-3 facilities at the University of Cagliari.

HuH7 cells were seeded at 10000 cells/well in 96-well cell-treated plates. The following day, cells were incubated with the control or compounds at different concentrations and the virus at MOI 1. Remdesivir was used as positive control. Cell monolayer was infected for 1 h at 37 °C, viral inoculum was removed and media with control or compounds serial dilution was freshly added. After 24 h, the supernatants were collected. At 24 h post-infection (hpi), viral RNA was extracted from the supernatant with the QIAamp Viral RNA Mini Kit (Qiagen) following manufacturer instructions. One-step RT-qPCR was performed to detect WNV Envelope gene copy number using the primers: forward GCAGCATTGGCAAAGCCTTTAC; reverse CTTGATGGACAGCCTTC CCAAC with Luna Universal One-Step RT-qPCR Kit (New England Biolabs) according to manufacturer's instructions in a CFX-96 RT-PCR (Biorad). Results report the mean and standard deviation of two independent biological replicates in duplicates. The Half maximal effective concentration (EC_{50}) value of the compound was calculated by normalizing the treated samples as percentage of the infected untreated samples, then by fitting the data to a dose-response curve (log_{10} concentration versus normalized response, variable slope) using non-linear regression in GraphPad Prism version 10.

Evaluation of compound cytotoxicity in HuH-7 cell line. HuH7 cells were seeded at 10000 cells/well in 96-well cell-treated plates. The following day, cells were incubated with the control or compounds at different concentrations. After 24 h post-treatment, 20 μl of 3-(4,5-dimethylthiazol-2-yl)-2,5-diphenyl-2H-tetrazolium bromide (MTT) dissolved in PBS at 7.5 mg/ml, were added to each well and the cells were incubated at 37 °C with 5% CO_2 for 1 h. After removal of the supernatant, cells were lysed with 100 μl/well of lysis buffer (100% 2-Propanol, 4% Triton-X-100, 0.4% Hydrogen Chloride) until the formazan crystals were completely dissolved. Absorbance was read at 570 nm with a plate reader (Victor Nivo, PerkinElmer). The half-maximal cytotoxic concentration (CC_{50}) value of the compound was calculated by fitting the data to a dose-response curve (log_{10} concentration versus normalized response, variable slope) using non-linear regression in GraphPad Prism version 10.

Evaluation of inhibition of ZIKV replication in Vero E6-GFP cells measuring viral cytopathic effect. The African green monkey kidney cell line, previously engineered to constitutively express GFP (Vero E6-GFP), was kindly provided by Janssen Pharmaceutical. Cells were maintained in Dulbecco's modified Eagle's medium (DMEM; Gibco) supplemented with 10% v/v fetal beef serum (FBS; Gibco), 0.075% sodium bicarbonate (7.5% solution, Gibco), and 1× Pen-strep (Euroclone) and kept under 5% CO2 at 37 °C. ZIKV strain MR766 was provided by EVA propagated in the mosquito-derived C6/36 cell line.

Cells were seeded at 10000 cells/well in 96-well plates. The following day, cells were treated with serial dilutions of the test compounds, all prepared in culture medium containing 2 μM of the P-gp inhibitor CP-100356 and infected with a TD_{80} of virus previously determined at 96 h. Remdesivir was used as a positive control. At 96 hpi, the media was removed, and the total well GFP fluorescence was measured with a Victor 3 with 485/535 nm excitation wavelength. The inhibition of viral replication was calculated as the percentage of the viral-induced cytopathic effect on infected untreated controls, using Prism 10 via non-linear regression.

Evaluation of compound cytotoxicity in Vero E6-GFP cell line. Vero E6-GFP cells were seeded at 10000 cells/well in 96-well plates; the following day, cells were treated with serial dilutions of the test compounds, all prepared in culture medium containing 2 μM of the P-gp inhibitor CP-100356. At 96 h post-treatment, the media was removed and the total well GFP fluorescence was measured with a Victor 3 with 485/535 nm excitation wavelength. The cytotoxicity was calculated as the percentage of fluorescence of untreated controls.

CRediT authorship contribution statement

Antonio Lupia: Writing – original draft, Methodology, Data curation, Conceptualization. **Salvatore Nieddu:** Writing – original draft, Investigation, Data curation. **Laura Demuru:** Writing – review & editing, Investigation. **Erica Sanna:** Writing – review & editing, Investigation. **Alessia Onali:** Writing – review & editing, Investigation. **Roberta Emmolo:** Writing – review & editing, Investigation. **Paolo Malune:** Writing – review & editing, Investigation. **Simona Distinto:** Writing – review & editing, Supervision, Software, Data curation. **Giulia Atzeni:** Writing – review & editing, Investigation. **Annalaura Paulis:** Writing – review & editing, Investigation. **Rita Meleddu:** Writing – review & editing, Resources. **Filippo Cottiglia:** Writing – review & editing. **Francesca Esposito:** Writing – review & editing, Methodology. **Angela Corona:** Writing – review & editing, Methodology, Data curation. **Sharon D. Bryant:** Writing – review & editing, Software. **Elias Maccioni:** Writing – review & editing, Supervision. **Enzo Tramontano:** Writing – review & editing, Supervision, Resources, Conceptualization.

Declaration of competing interest

The authors declare that they have no known competing financial interests or personal relationships that could have appeared to influence the work reported in this paper.

Acknowledgments

This research was supported by START-UP Project MUR D.M. 737/2021- Intervention line "Interdisciplinary research initiatives on cross-cutting topics of relevance for the National Recovery Plan (PNRR)-Next Generation EU.

Authors thank Janssen Pharmaceutical for providing the African green monkey kidney Vero E6-GFP cell line that was engineered to constitutively express GFP.

Giulia Atzeni is granted by National PhD Programme in One Health approaches to infectious diseases and life science research, Department of Public Health, Experimental and Forensic Medicine, University of Pavia, Pavia, 27100, Italy.

The authors express their gratitude to Thierry Langer of the Department of Pharmaceutical Chemistry, Faculty of Life Sciences, University of Vienna.

Appendix A. Supplementary data

Supplementary data to this article can be found online at https://doi.org/10.1016/j.ejmech.2026.119306.

Abbreviations

AMC	7-amino-4-methylcoumarin
AUC	area under the curve
CADD	computer-aided drug design
CHAPS	3-[(3-cholamidopropyl)dimethylammonio]-1-propanesulfonate
CHIKV	chikungunya virus
cMD	conventional molecular dynamics
CC_{50}	half-maximal cytotoxic concentration
CP	compound
CPU	central processing unit
CV	coefficient of variation
DENV	dengue virus
DMEM	Dulbecco's modified Eagle medium
DMSO	dimethyl sulfoxide
DSF	differential scanning fluorimetry
EC_{50}	half-maximal effective concentration
ER	endoplasmic reticulum
EVA	European Virus Archive
FAM	fluorescein amidite
FBS	fetal bovine serum
FBS-HI	heat-inactivated fetal bovine serum
FDA	U.S. Food and Drug Administration
FP	false positives
GBS	Guillain-Barré syndrome
GFP	green fluorescent protein
GPU	graphics processing unit
GUI	graphical user interface
H	hydrophobic (pharmacophore feature)
HBA	hydrogen-bond acceptor
HBD	hydrogen-bond donor
HIV-1	human immunodeficiency virus type 1
hpi	hours post-infection
HSV1	herpes simplex virus 1
IC_{50}	half-maximal inhibitory concentration
IPTG	isopropyl-β-D-1-thiogalactopyranoside
JEV	Japanese encephalitis virus
K_i	inhibition constant
K_m	Michaelis constant
KNIME	Konstanz Information Miner
LB	lysogeny broth
MD	molecular dynamics
MOI	multiplicity of infection
MRC	multiple receptor conformation
MTT	3-(4,5-dimethylthiazol-2-yl)-2,5-diphenyl-2H-tetrazolium bromide
MUT	mutated
NPT	constant number of particles, pressure, and temperature
NTA	nitrilotriacetic acid
NTP	nucleoside triphosphate
OD_{600}	optical density at 600 nm
OPLS	optimized potentials for liquid simulations
PBVS	pharmacophore-based virtual screening
PBS	phosphate-buffered saline
PDB	Protein Data Bank
PI3K/Akt	phosphoinositide 3-kinase/protein kinase B
PME	particle mesh Ewald
PMSF	phenylmethylsulfonyl fluoride
PRCG	Polak-Ribière conjugate gradient
QSAR	quantitative structure–activity relationship
RMSD	root-mean-square deviation
ROC,	receiver operating characteristic
RPM	representative pharmacophore model
RT-qPCR	reverse transcription quantitative polymerase chain reaction
SARS-CoV-2	severe acute respiratory syndrome coronavirus 2
SB	structure-based
SD	standard deviation
SDS-PAGE	sodium dodecyl sulfate–polyacrylamide gel electrophoresis
SI	selectivity index
SP	standard precision
STING	stimulator of interferon genes
TD_{80}	80% tissue culture infective dose
TIP3P	transferable intermolecular potential with 3 points
TP	true positives
Vmax	maximum reaction velocity
VMD	visual molecular dynamics
VS	virtual screening
WT	wild-type
WHO	World Health Organization
WNV	West Nile virus
XVOL,	exclusion volume sphere
YFV	yellow fever virus
ZIKV	Zika virus

Data availability

Data will be made available on request.

References

[1] S. Du, et al., Aedes mosquitoes acquire and transmit Zika virus by breeding in contaminated aquatic environments, Nat. Commun. 10 (1) (Mar 22 2019) 1324, https://doi.org/10.1038/s41467-019-09256-0 (in eng).

[2] N. Vasilakis, S.C. Weaver, Flavivirus transmission focusing on Zika, Curr. Opin. Virol. 22 (Feb 2017) 30–35, https://doi.org/10.1016/j.coviro.2016.11.007 (in eng).

[3] G. Gutiérrez-Bugallo, et al., Vector-borne transmission and evolution of Zika virus, Nat. Ecol. Evol. 3 (4) (Apr 2019) 561–569, https://doi.org/10.1038/s41559-019-0836-z (in eng).

[4] O.J.M. Nascimento, I.R.F. da Silva, Guillain-Barré syndrome and Zika virus outbreaks, Curr. Opin. Neurol. 30 (5) (Oct 2017) 500–507, https://doi.org/10.1097/WCO.0000000000000471 (in eng).

[5] G.R. Deshpande, et al., An outbreak of Zika virus in Western India in the metropolis of Pune in the monsoon of 2024, J. Infect. Public Health 18 (5) (May 2025) 102720, https://doi.org/10.1016/j.jiph.2025.102720 (in eng).

[6] V.M. Cao-Lormeau, et al., Guillain-Barré Syndrome outbreak associated with Zika virus infection in French Polynesia: a case-control study, Lancet 387 (10027) (Apr 09 2016) 1531–1539, https://doi.org/10.1016/S0140-6736(16)00562-6 (in eng).

[7] D.W. Smith, J. Mackenzie, Zika virus and Guillain-Barré syndrome: another viral cause to add to the list, Lancet 387 (10027) (Apr 09 2016) 1486–1488, https://doi.org/10.1016/S0140-6736(16)00564-X (in eng).

[8] L.S. Muñoz, P. Barreras, C.A. Pardo, Zika virus-associated neurological disease in the adult: Guillain-Barré Syndrome, encephalitis, and myelitis, Semin. Reprod. Med. 34 (5) (Sep 2016) 273–279, https://doi.org/10.1055/s-0036-1592066 (in eng).

[9] L. López-Hortas, P. Pérez-Larrán, M.J. González-Muñoz, E. Falqué, H. Domínguez, Recent developments on the extraction and application of ursolic acid. A review, Food Res. Int. 103 (2018) 130–149, https://doi.org/10.1016/j.foodres.2017.10.028 (in eng).

[10] I. Abbas, F. Ahmed, H. Muqaddas, A. Alberti, A. Varcasia, L. Sedda, Epidemiology and surveillance of West Nile virus in the Mediterranean Basin during 2010-2023: a systematic review, Curr Res Parasitol Vector Borne Dis 7 (2025) 100277, https://doi.org/10.1016/j.crpvbd.2025.100277 (in eng).

[11] J.C. Saiz, M.A. Martín-Acebes, A.B. Blázquez, E. Escribano-Romero, T. Poderoso, N. Jiménez de Oya, Pathogenicity and virulence of West Nile virus revisited eight decades after its first isolation, Virulence 12 (1) (Dec 2021) 1145–1173, https://doi.org/10.1080/21505594.2021.1908740 (in eng).

[12] C. Nitsche, S. Holloway, T. Schirmeister, C.D. Klein, Biochemistry and medicinal chemistry of the dengue virus protease, Chem. Rev. 114 (22) (Nov 26 2014) 11348–11381, https://doi.org/10.1021/cr500233q (in eng).

[13] S.A. Shiryaev, P. Cieplak, A. Cheltsov, R.C. Liddington, A.V. Terskikh, Dual function of Zika virus NS2B-NS3 protease, PLoS Pathog. 19 (11) (Nov 2023) e1011795, https://doi.org/10.1371/journal.ppat.1011795 (in eng).

[14] N.J. Braun, et al., Structure-based macrocyclization of substrate analogue NS2B-NS3 protease inhibitors of Zika, west Nile and Dengue viruses, ChemMedChem 15 (15) (Aug 05 2020) 1439–1452, https://doi.org/10.1002/cmdc.202000237 (in eng).

[15] H. Lee, et al., Identification of novel small molecule inhibitors against NS2B/NS3 serine protease from Zika virus, Antivir. Res. 139 (Mar 2017) 49–58, https://doi.org/10.1016/j.antiviral.2016.12.016 (in eng).

[16] Q. Li, C. Kang, Structure and dynamics of zika virus protease and its insights into inhibitor design, Biomedicines 9 (8) (Aug 19 2021), https://doi.org/10.3390/biomedicines9081044 (in eng).

[17] Q. Ding, et al., Species-specific disruption of STING-dependent antiviral cellular defenses by the Zika virus NS2B3 protease, Proc. Natl. Acad. Sci. U. S. A. 115 (27) (Jul 03 2018) E6310–E6318, https://doi.org/10.1073/pnas.1803406115 (in eng).

[18] C. Kang, et al., Exploring the binding of peptidic West Nile virus NS2B-NS3 protease inhibitors by NMR, Antivir. Res. 97 (2) (Feb 2013) 137–144, https://doi.org/10.1016/j.antiviral.2012.11.008 (in eng).

[19] A. Poulsen, C. Kang, T.H. Keller, Drug design for flavivirus proteases: what are we missing? Curr. Pharm. Des. 20 (21) (2014) 3422–3427, https://doi.org/10.2174/13816128113199990633 (in eng).

[20] C. Nitsche, Proteases from dengue, West Nile and Zika viruses as drug targets, Biophys. Rev. 11 (2) (Apr 2019) 157–165, https://doi.org/10.1007/s12551-019-00508-3 (in eng).

[21] N.P. Santos, et al., Characterization of an allosteric pocket in zika virus NS2B-NS3 protease, J. Chem. Inf. Model. 62 (4) (Feb 28 2022) 945–957, https://doi.org/10.1021/acs.jcim.1c01326 (in eng).

[22] D. Luo, et al., Flexibility between the protease and helicase domains of the dengue virus NS3 protein conferred by the linker region and its functional implications, J. Biol. Chem. 285 (24) (Jun 11 2010) 18817–18827, https://doi.org/10.1074/jbc.M109.090936 (in eng).

[23] A.E. Aleshin, S.A. Shiryaev, A.Y. Strongin, R.C. Liddington, Structural evidence for regulation and specificity of flaviviral proteases and evolution of the Flaviviridae fold, Protein Sci. 16 (5) (May 2007) 795–806, https://doi.org/10.1110/ps.072753207 (in eng).

[24] C. Nitsche, et al., Peptide-Boronic acid inhibitors of flaviviral proteases: medicinal chemistry and structural biology, J. Med. Chem. 60 (1) (Jan 12 2017) 511–516, https://doi.org/10.1021/acs.jmedchem.6b01021 (in eng).

[25] M.R. Berthold, et al., KNIME-the Konstanz information miner: version 2.0 and beyond, AcM SIGKDD explorations Newsletter 11 (1) (2009) 26–31.

[26] M.A. Andrade, et al., Identification of novel Zika virus NS3 protease inhibitors with different inhibition modes by integrative experimental and computational approaches, Biochimie 212 (Sep 2023) 143–152, https://doi.org/10.1016/j.biochi.2023.04.004 (in eng).

[27] S.A. Shiryaev, et al., Characterization of the Zika virus two-component NS2B-NS3 protease and structure-assisted identification of allosteric small-molecule antagonists, Antivir. Res. 143 (Jul 2017) 218–229, https://doi.org/10.1016/j.antiviral.2017.04.015 (in eng).

[28] A.P. Bento, et al., The ChEMBL bioactivity database: an update, Nucleic Acids Res. 42 (Database issue) (Jan 2014) D1083–D1090, https://doi.org/10.1093/nar/gkt1031 (in eng).

[29] A. Gaulton, et al., ChEMBL: a large-scale bioactivity database for drug discovery, Nucleic Acids Res. 40 (Database issue) (Jan 2012) D1100–D1107, https://doi.org/10.1093/nar/gkr777 (in eng).

[30] M. Wieder, et al., Common hits approach: combining pharmacophore modeling and molecular dynamics simulations, J. Chem. Inf. Model. 57 (2) (Feb 27 2017) 365–385, https://doi.org/10.1021/acs.jcim.6b00674 (in eng).

[31] M.L. Peach, M.C. Nicklaus, Combining docking with pharmacophore filtering for improved virtual screening, J. Cheminf. 1 (1) (May 20 2009) 6, https://doi.org/10.1186/1758-2946-1-6 (in eng).

[32] J. Dong, X. Hao, Pharmacophore screening, molecular docking, and MD simulations for identification of VEGFR-2 and c-Met potential dual inhibitors, Front. Pharmacol. 16 (2025) 1534707, https://doi.org/10.3389/fphar.2025.1534707 (in eng).

[33] S. Tian, H. Sun, Y. Li, P. Pan, D. Li, T. Hou, Development and evaluation of an integrated virtual screening strategy by combining molecular docking and pharmacophore searching based on multiple protein structures, J. Chem. Inf. Model. 53 (10) (Oct 28 2013) 2743–2756, https://doi.org/10.1021/ci400382r (in eng).

[34] A. Faris, et al., Revealing innovative JAK1 and JAK3 inhibitors: a comprehensive study utilizing QSAR, 3D-Pharmacophore screening, molecular docking, molecular dynamics, and MM/GBSA analyses, Front. Mol. Biosci. 11 (2024) 1348277, https://doi.org/10.3389/fmolb.2024.1348277 (in eng).

[35] S. Yoon, W.J. Welsh, Identification of a minimal subset of receptor conformations for improved multiple conformation docking and two-step scoring, J. Chem. Inf. Comput. Sci. 44 (1) (2004) 88–96, https://doi.org/10.1021/ci0341619 (in eng).

[36] A.M. Ferrari, B.Q. Wei, L. Costantino, B.K. Shoichet, Soft docking and multiple receptor conformations in virtual screening, J. Med. Chem. 47 (21) (Oct 07 2004) 5076–5084, https://doi.org/10.1021/jm049756p (in eng).

[37] G. Robin, et al., Structure of West Nile virus NS3 protease: ligand stabilization of the catalytic conformation, J. Mol. Biol. 385 (5) (Feb 06 2009) 1568–1577, https://doi.org/10.1016/j.jmb.2008.11.026 (in eng).

[38] S.R. Radoshitzky, et al., Expanded profiling of Remdesivir as a broad-spectrum antiviral and low potential for interaction with other medications in vitro, Sci. Rep. 13 (1) (Feb 23 2023) 3131, https://doi.org/10.1038/s41598-023-29517-9 (in eng).

[39] C. Yung-Chi, W.H. Prusoff, Relationship between the inhibition constant (KI) and the concentration of inhibitor which causes 50 per cent inhibition (I50) of an enzymatic reaction, Biochem. Pharmacol. 22 (23) (1973) 3099–3108.

[40] N.N. Kalu, P.J. Desai, C.M. Shirley, W. Gibson, P.A. Dennis, R.F. Ambinder, Nelfinavir inhibits maturation and export of herpes simplex virus 1, J. Virol. 88 (10) (May 2014) 5455–5461, https://doi.org/10.1128/JVI.03790-13 (in eng).

[41] S. Bhakat, L. Delang, S. Kaptein, J. Neyts, P. Leyssen, V. Jayaprakash, Reaching beyond HIV/HCV: Nelfinavir as a potential starting point for broad-spectrum protease inhibitors against dengue and chikungunya virus, RSC Adv. 5 (104) (2015) 85938–85949.

[42] Z. Xu, et al., Preventive and therapeutic benefits of nelfinavir in rhesus macaques and human beings infected with SARS-CoV-2, Signal Transduct. Targeted Ther. 8 (1) (2023) 169.

[43] S. Wang, et al., Screening of FDA-approved drugs for inhibitors of Japanese encephalitis virus infection, J. Virol. 91 (21) (2017), https://doi.org/10.1128/jvi.01055-17.

[44] J.A. Bernatchez, L.T. Tran, J. Li, Y. Luan, J.L. Siqueira-Neto, R. Li, Drugs for the treatment of zika virus infection, J. Med. Chem. 63 (2) (Jan 23 2020) 470–489, https://doi.org/10.1021/acs.jmedchem.9b00775 (in eng).

[45] G. Madhavi Sastry, M. Adzhigirey, T. Day, R. Annabhimoju, W. Sherman, Protein and ligand preparation: parameters, protocols, and influence on virtual screening enrichments, J. Comput. Aided Mol. Des. 27 (3) (2013) 221–234.

[46] W.L. Jorgensen, D.S. Maxwell, J. Tirado-Rives, Development and testing of the OPLS all-atom force field on conformational energetics and properties of organic liquids, J. Am. Chem. Soc. 118 (45) (1996) 11225–11236.

[47] D.S. Wishart, et al., DrugBank 5.0: a major update to the DrugBank database for 2018, Nucleic Acids Res. 46 (D1) (2018) D1074–D1082.

[48] I.-J. Chen, N. Foloppe, Drug-like bioactive structures and conformational coverage with the LigPrep/ConfGen suite: comparison to programs MOE and catalyst, J. Chem. Inf. Model. 50 (5) (2010) 822–839.

[49] K.J. Bowers, et al., Scalable algorithms for molecular dynamics simulations on commodity clusters, in: Proceedings of the 2006 ACM/IEEE Conference on Supercomputing, 2006, pp. 84–es.

[50] W.L. Jorgensen, J. Chandrasekhar, J.D. Madura, R.W. Impey, M.L. Klein, Comparison of simple potential functions for simulating liquid water, J. Chem. Phys. 79 (2) (1983) 926–935.
[51] T. Darden, D. York, L. Pedersen, Particle mesh Ewald: an N log (N) method for Ewald sums in large systems, J. Chem. Phys. 98 (12) (1993) 10089–10092.
[52] W. Humphrey, A. Dalke, K. Schulten, VMD: visual molecular dynamics (in eng), J. Mol. Graph. 14 (1) (Feb 1996), https://doi.org/10.1016/0263-7855(96)00018-5, pp. 33–8, 27-28.
[53] B.J. Frey, D. Dueck, Clustering by passing messages between data points, Science 315 (5814) (Feb 16 2007) 972–976, https://doi.org/10.1126/science.1136800 (in eng).
[54] S.D. Roughley, Five years of the KNIME Vernalis cheminformatics community contribution, Curr. Med. Chem. 27 (38) (2020) 6495–6522, https://doi.org/10.2174/0929867325666180904113616 (in eng).
[55] G. Wolber, T. Langer, LigandScout: 3-D pharmacophores derived from protein-bound ligands and their use as virtual screening filters, J. Chem. Inf. Model. 45 (1) (2005 Jan-Feb 2005) 160–169, https://doi.org/10.1021/ci049885e (in eng).
[56] R.A. Friesner, et al., Glide: a new approach for rapid, accurate docking and scoring. 1. Method and assessment of docking accuracy, J. Med. Chem. 47 (7) (Mar 2004) 1739–1749, https://doi.org/10.1021/jm0306430 (in eng).